

# Interfacial thermal resistance in phonon hydrodynamic heat conduction

Cite as: J. Appl. Phys. 131, 064302 (2022); doi: 10.1063/5.0080688

Submitted: 2 December 2021 · Accepted: 25 January 2022 ·

Published Online: 10 February 2022



Ben-Dian Nie  and Bing-Yang Cao 

## AFFILIATIONS

Key Laboratory for Thermal Science and Power Engineering of Ministry of Education, Department of Engineering Mechanics, Tsinghua University, Beijing 100084, China

<sup>a)</sup>Author to whom correspondence should be addressed: caoby@tsinghua.edu.cn

## ABSTRACT

Two-dimensional materials are usually predicted to have ultrahigh thermal conductivity because of the numerous phonon normal scatterings, which might cause hydrodynamic heat conduction. In addition, boundary and interface are significant in the polycrystalline structure and material contacts. Therefore, this article investigates the thermal behaviors at the boundary and interface in phonon hydrodynamics. Monte Carlo simulation is adopted to study the heat conduction phenomena in Poiseuille hydrodynamics and Ziman hydrodynamics. The concept of a boundary temperature step is defined to depict the temperature decline behaviors at the boundary in steady hydrodynamic heat conduction. Interfacial thermal behaviors can be treated as a combination of the boundary effects and phonon transmission effects, where the interface properties can be described by the interface transmissivity and the specular reflectivity. Moreover, the inverse temperature difference at the interface is observed, which means that the heat is transported from low temperature to high temperature, implying that the definition of temperature in phonon hydrodynamic heat conduction ought to be further investigated. Then, two theoretical models are proposed to describe these phenomena, namely, the particle propagation model and the dual boundary flux model. The particle propagation model tries to trace the propagation and evolution of phonons with simpler rules, and it finds that the heat flux reduction originates from the backward phonons that are scattered by the normal scattering process. The dual boundary flux model divides the whole boundary heat flux into the hydrodynamic heat flux and the diffusive heat flux, and the boundary temperature step appears in the transition between these two fluxes. These two models are compared with the results obtained by Monte Carlo simulations.

Published under an exclusive license by AIP Publishing. <https://doi.org/10.1063/5.0080688>

## I. INTRODUCTION

Two-dimensional materials, especially graphene, attract lots of attention because of their excellent intrinsic physical properties, such as mechanical and thermal characteristics.<sup>1–4</sup> The thermal conductivity of monolayer graphene is demonstrated to be very high even at room temperature<sup>5</sup> thanks to the contribution of collective phonon motion.<sup>6–11</sup> According to whether the phonon momentum is conserved in the scattering process, phonon collisions can be classified as the normal scattering process (N process) and the Umklapp scattering process (U process).<sup>12</sup> In the N process, the phonon momentum is conserved after being scattered, while in the U process, it is not. The resistance scattering process (R process) is named to include all the scattering processes that destroy the phonon momentum.<sup>8</sup> If the N process dominates the phonon transport, phonon hydrodynamic heat conduction<sup>4,6,9,13–25</sup> appears, where many fascinating physical phenomena occur, such

as the phonon Poiseuille flow,<sup>26,27</sup> size-dependent thermal conductivity,<sup>28,29</sup> and second sound.<sup>30–39</sup> More specifically, phonon hydrodynamic transport can be classified into the Poiseuille hydrodynamics where the influences of the R process can be ignored, and the Ziman hydrodynamics where the R process plays a relatively important role besides the N process.<sup>8</sup> Two-dimensional materials usually have a high Debye temperature and a large amount of flexural mode phonons, which is thought to restrict the Umklapp scattering process in phonon collisions and strengthen the normal scattering process.<sup>16,40–42</sup> In these materials, the normal scattering rate is usually higher than the resistance scattering rate at not a very low temperature.<sup>8</sup> Therefore, they have relatively large hydrodynamic windows even at room temperature. Moreover, the second sound<sup>37</sup> and lattice cooling<sup>38</sup> are reported to be observed in highly oriented pyrolytic graphite at a temperature as high as 100 K, breaking the conventional recognition that the phonon

hydrodynamic heat conduction can be only observed under an ultralow temperature.

The phonon normal scattering process does not produce thermal resistance itself but influences the thermal conductivity via the interactions with other mechanisms, such as boundary scattering and Umklapp scattering.<sup>43</sup> The ignorance of the normal scattering process would underestimate the thermal conductivity.<sup>12</sup> Callaway<sup>12</sup> derived the thermal conductivity models with frequency-dependent relaxation times based on the dual relaxation time approximation method, and then, Allen<sup>44</sup> improved it with a more rigorous treatment of phonon–phonon scattering. Alvarez *et al.*<sup>45</sup> thought that it was important to change the way to perform the average on the scattering rates and they developed the kinetic collective model to predict the thermal conductivity when the N process was important. Meanwhile, the boundary scatterings destroy the phonon momentum, also producing thermal resistance.<sup>46–48</sup> Poiseuille flow arises just because of the boundary scatterings parallel with the direction of heat flow.<sup>26,27</sup> Moreover, the size-dependent thermal conductivity was also different from the linear relation predicted by the ballistic heat transport.<sup>28</sup> Lee<sup>29</sup> demonstrated that there was entropy production in the transition of phonon distribution from non-collective to collective, corresponding to the boundary thermal resistance.

Interfacial thermal resistance<sup>49–57</sup> plays a significant part in non-Fourier heat conduction phenomena, such as ballistic heat transport and hydrodynamic heat transport. Several theoretical models are proposed to predict the boundary thermal conductance (or so-called interfacial thermal resistance), such as the Acoustic Mismatch Model<sup>58,59</sup> (AMM), where the phonons at the interface are transported in a specular behavior, and the Diffusive Mismatch Model<sup>49</sup> (DMM), where the phonons at the interface are scattered diffusively. Frank *et al.*<sup>60–62</sup> investigated in detail the thermal resistance at the solid–liquid interface via molecular dynamics and found that the influences of solid–liquid interaction strength on the thermal resistance were rather complex. By controlling the roughness of the interface, they found that the thermal resistance was contributed by two factors,<sup>62</sup> the area of the solid–liquid interface and the vibrational anharmonicity. Moreover, the interface might alter the phonon properties in the individual materials so that the bulk properties are not applicable anymore.<sup>55</sup> Hua and Minnich<sup>63</sup> solved the frequency-dependent Boltzmann transport equation semi-analytically and depicted the heat conduction patterns from a diffusive to a ballistic regime in this film. Hao *et al.*<sup>64</sup> studied the ballistic phonon resistance resulting from the size effect and provided a new approach to extract the effective phonon mean free path (MFP) distribution for the in-plane heat conduction. As for the various non-Fourier heat conduction models, Lor and Chu<sup>50,65</sup> studied the transient non-Fourier heat conduction behaviors when thermal waves propagated across the interface by adopting the Cattaneo–Vernotte equation and found that the interfacial thermal resistance would change the interfacial temperature difference but maintain their profiles. Ho *et al.*<sup>66</sup> used the lattice Boltzmann method to investigate the heat transfer in multilayered materials within the framework of the dual-phase-lag (DPL) heat conduction model to show the temperature profiles after a heat pulse passed across an interface. Liu<sup>67</sup> analyzed metal films using the hyperbolic microscopic two-step model and found that the hyperbolic nature

of heat in an electron gas significantly affects the thermal behaviors at early times. Al-Nimr *et al.*<sup>68–70</sup> investigated the DPL model for composite structures and considered the influence of the thermal boundary resistance, initial temperature, and material thermal properties on the thermal waves that are penetrating another media.

Phonon hydrodynamic heat transport, one of the non-Fourier heat conduction phenomena, is also influenced by the interfaces, which is very common in heat conduction in polycrystalline structures or composite materials. Nevertheless, little attention is paid to the steady heat conduction in phonon hydrodynamics with interfacial thermal resistance. In addition, some research studies are focused on the cross-plane interfacial thermal conductance of graphite. However, there is a lack of studies on the in-plane interfaces of two-dimensional materials, since the in-plane thermal conductivity of the two-dimensional materials is far higher than that of the cross-plane.<sup>71</sup> The two-dimensional materials, which are seen as the typical promising future materials, are deeply influenced by phonon normal scattering, and interfaces are unavoidable in the production and application of two-dimensional materials. Therefore, a profound understanding of the steady heat conduction phenomena and interfacial thermal resistance in phonon hydrodynamic heat conduction is significant.

This article aims to investigate the thermal behaviors at the interface in the phonon hydrodynamic regime. In Sec. II, the Monte Carlo (MC) simulation algorithm to solve the phonon Boltzmann equation is introduced. The steady temperature distribution profile is depicted and the boundary temperature step is named in Sec. III A, since the interfacial thermal resistance is highly related to the boundary thermal resistance. Then, the thermal behaviors at the interface are analyzed from the Monte Carlo simulation results. In Sec. IV, two simplified theoretical models for boundary influences and interfacial temperature characteristics are introduced.

## II. NUMERICAL METHODS AND SIMULATION DETAILS

### A. Phonon Boltzmann transport equation

The phonon Boltzmann transport equation depicts the transport behaviors of phonons in real space and phase space,

$$\begin{aligned} \iint_{V,K} \left[ \frac{\partial f(\mathbf{K}, x)}{\partial t} + v(\mathbf{K}, x) \nabla f(\mathbf{K}, x) \right] dV d\mathbf{K} \\ = \iint_{V,K} C f(\mathbf{K}, x) dV d\mathbf{K}, \end{aligned} \quad (1)$$

where  $f$ ,  $\mathbf{K}$ , and  $x$  are the phonon distribution function, phonon wavevector, and spatial coordinate, respectively, and  $C$  represents the collision operator. Many efforts are made to solve the collision term, such as by the relaxation time approximation (RTA) and by the full scattering matrix.<sup>72</sup> RTA regards that the phonons approach the equilibrium distribution after being scattered, which is demonstrated to be relatively accurate with properly selected parameters. Callaway<sup>12</sup> developed the dual relaxation time approximation method to emphasize the contribution of phonon normal

scattering in heat transport, where  $\tau_N$  and  $\tau_U$  are the relaxation times of the phonon normal scattering process (N process) and the Umklapp scattering process (U process), respectively,

$$Cf = \frac{f_0 - f}{\tau_U} + \frac{f_d - f}{\tau_N} = \left[ \left( \frac{\tau_U f_0}{\tau_U} + \frac{\tau_U f_d}{\tau_N} \right) - f \right] / \tau_t. \quad (2)$$

In Eq. (2),  $f_0$  and  $f_d$  represent the equilibrium Bose–Einstein distribution and displaced Bose–Einstein distribution, respectively, and  $\tau_t$  is the total relaxation time, defined by the Matthiessen rule as  $\tau_t^{-1} = \tau_N^{-1} + \tau_U^{-1}$ . Phonon Monte Carlo (MC) simulation algorithm based on the dual relaxation time approximation is adopted to solve the phonon Boltzmann transport equation, which has been described in detail in Ref. 20. One of the advantages is that this algorithm reduces the number of total particles and saves the memory and computational time.

Temperature is an important quantity in the simulation process defined based on local equilibrium assumption. However, in phonon hydrodynamics, the equilibrium phonon distribution is not the equilibrium Bose–Einstein distribution, but the displaced one, which is totally different from the diffusive heat conduction.<sup>7</sup> In this article, the concept of temperature is used by calculating the equilibrium temperature, which has the same thermal energy density  $e(T_0)$  with the given area, as shown in Eq. (3),

$$e(T) = \iint_{V, \mathbf{K}} \frac{\hbar\omega}{\exp\left(\frac{\hbar\omega}{kT_0}\right) - 1} dV d\mathbf{K} = e(T_0). \quad (3)$$

$T$  and  $T_0$  represent the hydrodynamic temperature and the equilibrium temperature, respectively. They are the same when the thermal energy densities are the same. In this way, the hydrodynamic temperature becomes a label of thermal energy density. Therefore, sometimes in this article, thermal energy density is used instead of temperature to depict the thermal behaviors in phonon hydrodynamics, where Eq. (3) is assumed. When the temperature change is small enough, it is regarded that there is a linear relationship between the thermal energy density difference  $\Delta E$  and the temperature difference  $\Delta T$ .

## B. Scattering process

The dual relaxation time approximation method is used to solve the collision term in Eq. (1) for the Monte Carlo simulations, as Eq. (2) shows. When the N process plays a major part, the phonon distribution approaches the displaced Bose–Einstein distribution while the U process leads to the equilibrium Planck distribution, where  $1/\tau_t = 1/\tau_U + 1/\tau_N$ . Thus, another parameter is defined to study the coupled effect of the N process and the U process, namely, resistance scattering probability  $M$ . It is a simulation parameter, meaning the probability of phonons to be scattered by the resistance scattering process. In this article, the resistance scattering process (R process) includes the Umklapp scattering process, defect scattering, isotopic scattering, and so on, except for boundary resistance, since boundary resistance is specifically studied. The definition of  $M$  comes from the ratio of the relaxation

times for the N and R processes,

$$M(\omega) = \frac{1}{\tau_R(\omega)} / \left( \frac{1}{\tau_N(\omega)} + \frac{1}{\tau_R(\omega)} \right). \quad (4)$$

As the relaxation times  $\tau_N$  and  $\tau_R$  are frequency dependent,  $M$  is frequency dependent as well.

In the MC algorithm, the phonons in the material are sampled and traced until they end their lives.<sup>73</sup> The stochastic method is adopted to derive the phonon life and travelling distance from  $\tau_t$ . The computer gives a random number  $R$  in the range from 0 to 1 and the travelling distance  $l$  is

$$l = -\lambda_t \ln(R), \quad (5)$$

where

$$\lambda_t = \tau_t v_g \quad (6)$$

is set to be the mean free path of phonons. The calculation regime is divided into several grids to count the energy and momentum. Since this algorithm adopts the concept of energy particles, instead of the phonon particles, the conservation of particle number is equal to the conservation of thermal energy. If the energy particles are judged to be scattered in the R process, their new properties are determined by the equilibrium Bose–Einstein distribution. Otherwise, their new properties are given from the displaced Bose–Einstein distribution. More algorithm details can be found in Ref. 20. In this way, the hydrodynamic heat conduction is simulated.

## C. Boundary conditions and interface properties

As mentioned above, two kinds of boundaries are analyzed in this article, namely, the adiabatic boundary and the emitting boundary. Since the adiabatic boundary has no interaction with the external thermal energy, it can only reflect the phonons that meet the boundary. The emitting boundary, also known as the absorbing boundary in MC simulation, gives external thermal energy import based on the temperature or the heat flux. The boundary emits phonons at a given rate and absorbs all the phonons that arrive. The direction distribution of these phonons follows the Lambert distribution,

$$I = I_0 \cos \theta, \quad (7)$$

where  $I$  represents the energy density. Lambert distribution means that the phonons are in thermal equilibrium. Thus, in the phonon hydrodynamic regime, the transition from equilibrium Bose–Einstein distribution to displaced equilibrium distribution can be observed. The probability density function  $P_\omega$  for phonon frequency can be written as

$$P_\omega(T) = \frac{\hbar\omega[f_0(\omega, T) - f_{ref}(\omega, T)]D(\omega)}{\int_K \hbar\omega[f_0(\omega, T) - f_{ref}(\omega, T)]D(\omega)d\omega}, \quad (8)$$

where  $f_{ref}$  is the reference equilibrium state, chosen according to the circumstance conditions.

Two parameters are adopted to characterize the interfacial thermal properties,<sup>57,74</sup> namely, the interface transmissivity  $t$  and the boundary specular reflectivity  $s$ . When phonons meet with the interface, they might be reflected or transmitted directly. The proportion of the phonons that could pass through the interface is named as the interface transmissivity  $t$ . When  $t=0$ , all the phonons are reflected to the original material. When  $t=1$ , the interface does not exist and all the phonons can propagate into the other material. The interface transmissivity for phonons from material I to II is  $t_{12}$ , and the transmissivity in the opposite direction is  $t_{21}$ . If I and II are the same materials, according to the detailed equilibrium, it can be inferred that

$$t_{12} = t_{21}. \tag{9}$$

Boundary specular reflectivity  $s$  represents the percentage of the phonons at the boundary that are reflected according to Fresnel's law, and it is dependent on the boundary roughness. If the boundary is smooth, the specular reflectivity is unity and all the phonons are reflected with the same phonon momentum parallel with the boundary. As for the phonon momentum perpendicular to the boundary, it is inverse. The phonon frequency follows the equilibrium Bose-Einstein distribution. If the boundary is coarse, the specular reflectivity is 0 and all the phonons are re-emitted according to the Lambert distribution. The polar angle of coarse boundary  $\theta$  is determined by

$$\cos \theta = 1 - 2R \tag{10}$$

and  $R$  is a random number given by the computer. In this way, the boundary heat flux parallel to the coarse boundary equals zero and the phonon Poiseuille flow comes into being.<sup>7</sup> Different sides of the interface have different boundary reflectivities  $s_1$  and  $s_2$ , and here,

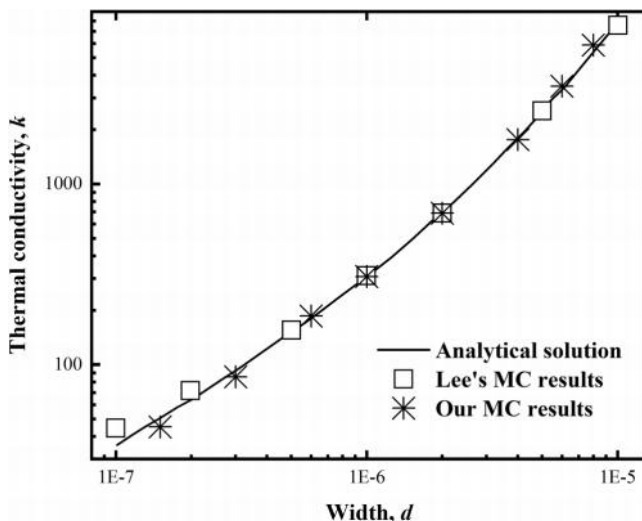


FIG. 1. Thermal conductivity in phonon hydrodynamic heat transport of the nanofilm with finite width and infinite length.

they are assumed to be the same, namely,  $s_1 = s_2$ . Both the reflected phonons and passing phonons have new frequencies, derived from the equilibrium Bose-Einstein distribution. In the simulation process, a random number  $R_t$  is given by the computer; if  $R_t < t$ , the phonon would pass through the interface. Otherwise, it is reflected. Then, another random number  $R_r$  is given. If  $R_r < r$ , the phonon will obey Fresnel's law, namely, the reflection law and the refraction law. Otherwise, the phonon wave vector is redistributed based on the Lambert distribution.

The MC simulation in this article has been verified. It can be shown from Fig. 1 that our results agree with previous research studies.<sup>29,47</sup> The semi-analytical solution is derived from reference. The rectangular is the result of Lee's algorithm and the asterisk is from our model. The Debye model is adopted in this simulation and the Debye temperature of the given material is set to be 1200 K and the initial temperature is 100 K. The relaxation time is  $10^{-10}$  s and the phonon group velocity is  $10^4$  m/s. Here, the width is finite while the length is infinite. The infinite length is achieved in the simulations by setting the length to be much larger than the width.

#### D. Calculation regime

The boundary behaviors in phonon hydrodynamics are investigated first, and then, the interfacial thermal behaviors between two individual nanofilms are analyzed, as shown in Fig. 2. When phonons meet the interface between the two nanofilms with the same material, interfacial interactions will reflect some phonons and allow the others to pass through. Two kinds of boundaries are analyzed here, namely, the emitting boundary and the adiabatic boundary. Emitting boundaries mean these boundaries with external energy input and output, including the isothermal boundary and heat flow boundary. Adiabatic boundaries have no energy exchange with the outside circumstance. However, it influences heat conduction by absorbing and reemitting phonons. If the boundaries are coarse, the phonon momentum would be destroyed, resulting in boundary thermal resistance.

Two individual cases based on the Debye model are analyzed in this article to study the boundary thermal resistance and interfacial thermal resistance. The MC algorithm is established in two-dimensional space. In case 1 [Fig. 2(a)], a nanofilm with finite length and infinite width is considered. Two temperature boundaries are set at the end of the lengths,  $T_1$  and  $T_2$ . If  $T_1 > T_2$ , the heat flux flows from the left to the right and boundary resistance

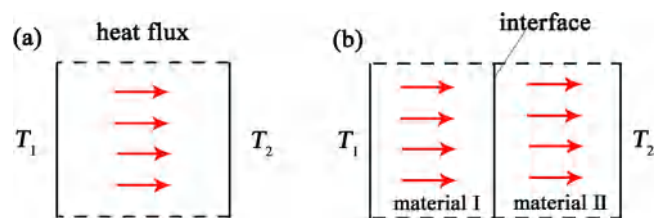


FIG. 2. Schematic diagrams for the two simulation cases. (a) Heat conduction with finite length and infinite width; (b) heat conduction through the interface between two individual nanofilms with finite length and infinite width.

appears. If there is no specific demonstration, the regime length is set to be 5000 nm and the initial temperature is 200 K. In case 2 [Fig. 2(b)], two nanofilms of the same material contact each other, constructing the interface, which determines whether the phonons would pass through or be reflected. The total length is 5000 nm while the interface is placed at the middle. The width boundaries are set to be periodic to simulate the infinite boundary condition. Since the Debye model is adopted, the phonon direction distribution is regarded as continuous and the direction of the wave vector is compatible with the velocity direction. Therefore, the U process distributes the phonon velocity direction evenly while the N process has a preferable direction along with the direction of drift velocity  $\mathbf{u}_d$ . In all the figures in this article, the total length  $L = 5000$  nm is normalized to 1 to make the expression simpler.

### III. INTERFACIAL BEHAVIORS IN STEADY POISEUILLE HYDRODYNAMIC HEAT CONDUCTION

For simplification, if there is no specific declaration, in this article, the hydrodynamic heat conduction means the Poiseuille hydrodynamic heat conduction, where the phonon normal scattering process is dominant and the phonon resistive scattering process can be ignored. In this section, the boundary effect and the interfacial behaviors in steady hydrodynamic heat conduction are depicted by the Monte Carlo simulations.

#### A. Boundary temperature step and entropy analyses

The temperature distribution in a nanofilm with finite length in phonon hydrodynamics has been calculated by Lee<sup>29</sup> and Liao.<sup>46</sup> Even though the N process causes no thermal resistance, near the boundary there are boundary temperature jump and *boundary temperature step*, which describes the temperature distributions between the temperature boundary and the middle part of the medium, as shown in Fig. 3. It can be found that the boundary influences, which result in the temperature gradient, decrease as the

distance from the boundary becomes larger. In the middle part of the medium, the boundary effects are negligible and there is no temperature gradient. Hence, parts A and C in Fig. 3 are called *boundary temperature steps*, both of which reflect the nonlinear temperature distribution related to the boundaries. Here, the concept of the *boundary temperature step difference* is used to describe the temperature difference between the temperature at the inner side of the boundary and the steady temperature in the middle part of the medium, denoting the step height, as shown in Fig. 3, which is plotted by Lee.<sup>29</sup> The given boundary temperature is the temperature at the outer side of the boundary, and the difference between which and the temperature at the inner side of the boundary is called boundary temperature jump.

The normal scattering process leads the phonons to the displaced Bose-Einstein distribution  $f_d$ ,

$$f_d = \frac{1}{\exp\left(\frac{\hbar\omega}{kT} - \frac{\hbar\mathbf{K} \cdot \mathbf{u}_d}{kT}\right) - 1}, \quad (11)$$

where  $\omega$ ,  $\mathbf{K}$ , and  $\mathbf{u}_d$  represent the phonon frequency, phonon wave vector, and the phonon drift velocity, respectively. Based on the expression [Eq. (11)], the phonons have a preference direction after being scattered, which is along with the direction of original momentum. In this way, the phonon momentum is conserved. The drift velocity  $\mathbf{u}_d$ , which has been demonstrated to be the same in all phonon branches,<sup>7</sup> influences both the phonon frequency and phonon wave vector. Here, several normalized quantities are defined to make the expression clearer. They are the nondimensional frequency  $m_\omega$ , which is the function of frequency  $\omega$  and temperature  $T$ , and the drift velocity ratio  $r$ ,

$$m_\omega = \frac{\hbar\omega}{kT}, \quad (12)$$

$$r = \left| \frac{\mathbf{u}_d}{\mathbf{v}_g} \right|. \quad (13)$$

$\mathbf{v}_g$  is the phonon group velocity. When the drift velocity ratio  $r$  and nondimensional frequency  $m_\omega$  are small enough ( $r < 0.2$ ,  $m < 5$ , empirically), the distribution Eq. (11) can be linearized with ignorable error as

$$f_d = \frac{1}{\exp\left(\frac{\hbar\omega}{kT}\right) - 1} + \frac{\exp\left(\frac{\hbar\omega}{kT}\right)}{\left[\exp\left(\frac{\hbar\omega}{kT}\right) - 1\right]^2} \frac{\hbar\mathbf{K} \cdot \mathbf{u}_d}{kT}. \quad (14)$$

Figure 4 compares the probability distribution function predicted by Eqs. (11) and (14), where the control variate method has been used. In Fig. 4(a), the drift velocity ratio  $r$  is 0.05 and the  $m_\omega$  varies at 0.1, 0.5, 1.0, and 5.0. When  $m_\omega = 5.0$ , the profiles predicted by Eqs. (11) and (14) appear to deviate. In Fig. 4(b), the nondimensional frequency  $m_\omega$  is set to be 1, and the drift velocity ratio  $r$  varies at 0.001, 0.01, 0.05, 1.0, 2.0, and 3.0.

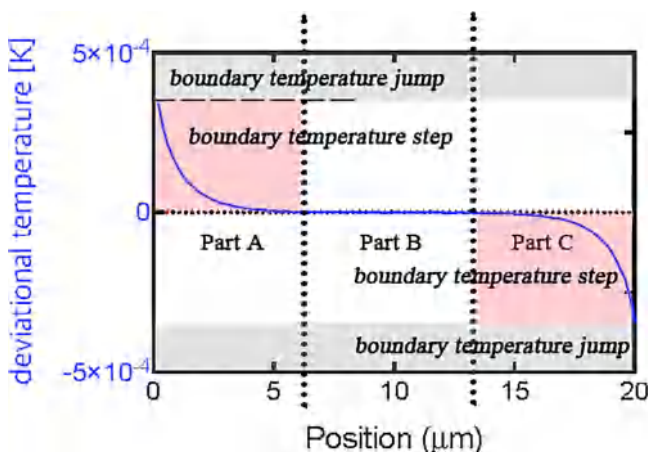


FIG. 3. The steady temperature profile in phonon hydrodynamic heat conduction for a nanofilm with finite length.<sup>29</sup>

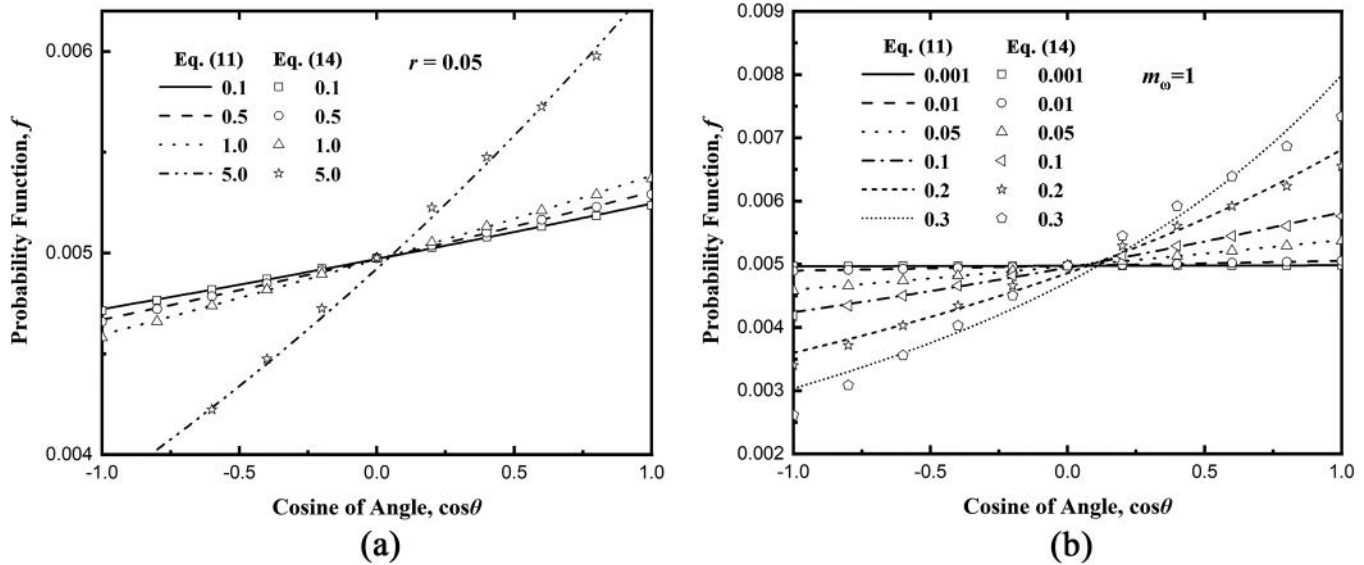


FIG. 4. Comparisons of the probability distribution function predicted by Eqs. (11) and (14) at different nondimensional frequency  $m_\omega$ , and drift velocity ratio  $r$ . (a)  $r = 0.05$  and the nondimensional frequency  $m_\omega$  varies between 0.1 and 5.0. (b)  $m_\omega = 1$  and the drift velocity ratio  $r$  varies between 0.001 and 0.3.

The phonons following the Bose–Einstein distribution propagate in all directions evenly and the total phonon momentum is zero. As shown in Fig. 4, the displaced Bose–Einstein distribution has a preference direction along with the drift velocity to make the total momentum conserved. These velocity directions are analyzed to reveal how thermal boundary resistance in phonon hydrodynamics is produced. It has been recognized that boundary resistance exists due to phonon distribution transition from the equilibrium Bose–Einstein distribution to the displaced one.

In a two-dimensional nanofilm with finite length and infinite width, two temperature boundaries with finite temperature differences are adopted. The higher temperature is 201 K and the lower temperature is 200 K. The regime length is set to be 5000 nm, and the gray model gives a uniform mean free path (MFP) for the N process. When the system comes to a steady state, the temperature distribution is plotted in Fig. 5. As the temperature is defined as the function of local energy density, the energy distribution has a similar tendency with temperature profiles. In Fig. 5, three kinds of phonon MFPs are considered,  $\lambda_N = 500, 1000,$  and  $1500$  nm, making  $Kn$  to be 0.1, 0.2, and 0.3, respectively.  $Kn$  is the ratio of the phonon MFP with respect to the characteristic length and is characterized by the MFP of the U process and the N process, respectively,

$$Kn_U = \frac{\lambda_U}{L}, \tag{15}$$

$$Kn_N = \frac{\lambda_N}{L}. \tag{16}$$

It was thought that there was no thermal resistance in the N process, so the temperature gradient was not supposed to exist.

However, it is demonstrated to be untrue because thermal resistance arises from the phonon distribution transition from non-collective to collective. Boundary temperature steps appear. However, ballistic heat conduction fails to describe this kind of phenomenon, as shown in Fig. 5. In the middle part of the nanofilm, there is no temperature gradient, and therefore, there is no thermal resistance in the middle part. In the area near the boundary, a gradually flattening slope exists. The temperature step difference at the left boundary is  $\Delta T_1$  and that at the right boundary is  $\Delta T_2$ , as shown in Figs. 5 and 6. At the high temperature boundary, the temperature step difference  $\Delta T_1$  is positive, while at the low temperature boundary, the temperature step difference ( $-\Delta T_2$ ) is negative. The absolute values of these two temperature step differences are not totally the same, but they all have relationships with  $Kn$ . Figure 6 shows the temperature profiles under heat flux boundaries, where the flux  $q_0$  is determined as

$$q_0 = 0.25 \rho C_V (T_1 - T_2) v_g. \tag{17}$$

In Eq. (17), 0.25 is the shape factor. At different MFPs, the left temperature slopes  $\Delta T_1$  are almost the same, while the right temperature slopes  $\Delta T_2$  are different. At the same time, the absolute values of  $\Delta T_1$  and  $\Delta T_2$  are not the same, either. Another observation is about the boundary penetration length. The penetration length of the temperature step is more than one MFP  $\lambda_N$ , as shown by the imaginary line. When  $Kn = 0.3$ , the whole nanofilm has been influenced. It implies that boundary influences generally exist in phonon hydrodynamics, no matter under temperature boundary or heat flux boundary.

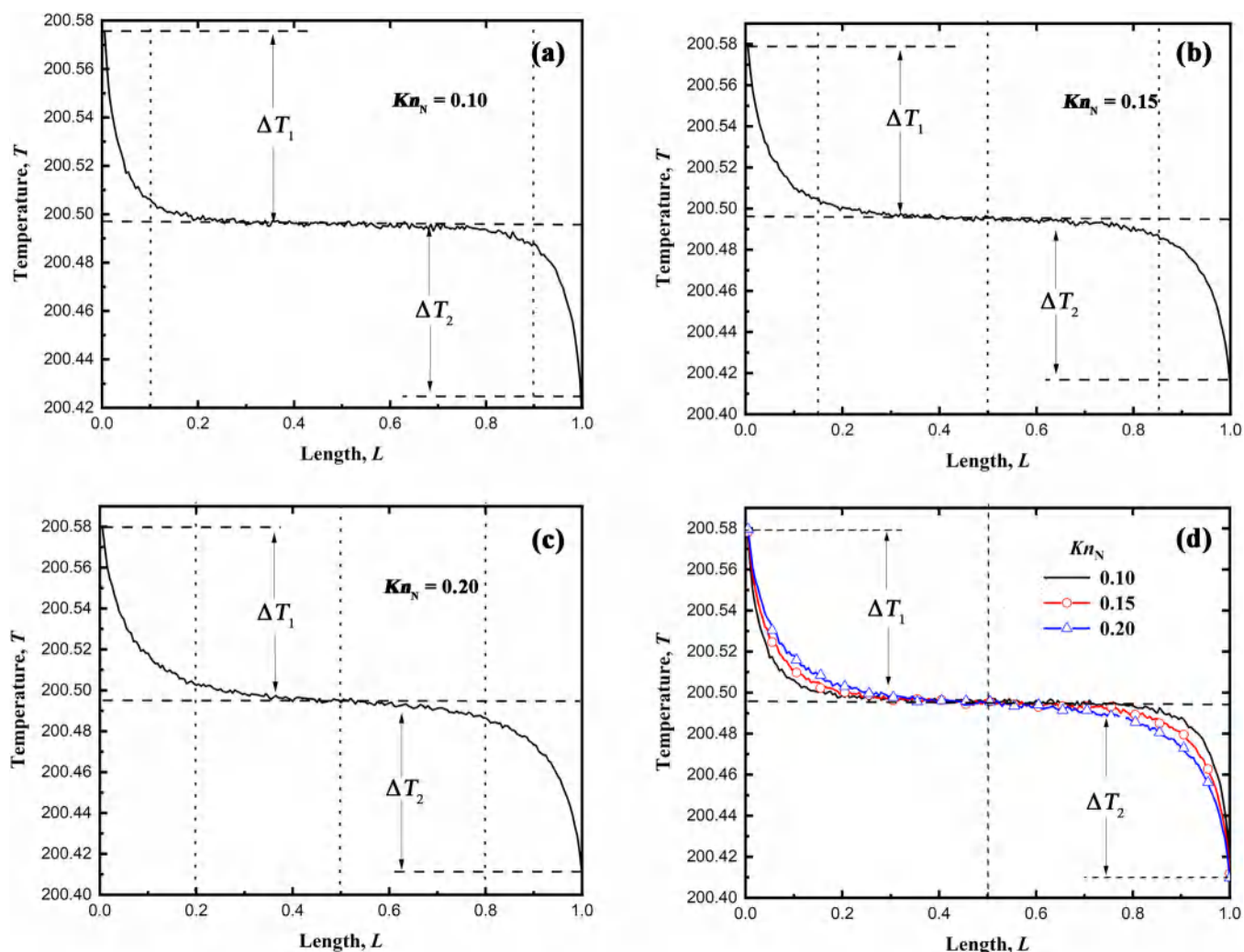


**FIG. 5.** When the temperature boundary is adopted, the steady temperature profile is depicted for the nanofilms with finite length in phonon hydrodynamics at different mean free paths, (a)  $\lambda_N = 500$  nm, (b)  $\lambda_N = 1000$  nm, (c)  $\lambda_N = 1500$  nm. (d) is the combination of the previous three figures.

## B. Phonon drift velocity and the generation of hydrodynamic boundary resistance

Drift velocity is an important quantity in phonon hydrodynamics.<sup>10</sup> As mentioned in Sec. III A, phonons in the hydrodynamic regime have an uneven velocity direction distribution in the momentum space. The velocity direction of phonons is represented by the polar angle and azimuth angle, as shown in the reference. Here, the cosine values of the phonon polar angle are plotted in Fig. 7. An obvious difference in the angle distribution between  $\cos \theta > 0$  and  $\cos \theta < 0$  can be found near the boundary, where  $x$  denotes the position. When  $x = 0.01$ , the right part in Fig. 7(a) is nearly even, while the left part is linear and a linear equation is derived based on the least square method. When  $x = 0.2$  [Fig. 7(b)], the  $\cos \theta > 0$  part gradually matches the equation with several

fluctuations and the left part is still linear. In the middle part  $x = 0.5$  [Fig. 7(c)], the phonon velocity direction distribution matches well with the given linear equation, giving a definite drift velocity. It can be found that the ratio of the drift velocity with respect to the phonon group velocity is 0.0091, much smaller than 0.1. It is also demonstrated that the linearization of the displaced Bose–Einstein distribution is proper in this case. At the right boundary,  $x = 1.0$  [Fig. 7(d)], the left part of the distribution is even while the right part is linear, just the other way around, compared with  $x = 0.01$ . From the view of phonon propagation, when  $\cos \theta > 0$  (polar angle  $\theta > 0$ ), the phonons propagate from the left to the right and vice versa. At the left boundary, the phonons from the left to the right follow the equilibrium Bose–Einstein distribution, while those from the right to the left obey the displaced Bose–

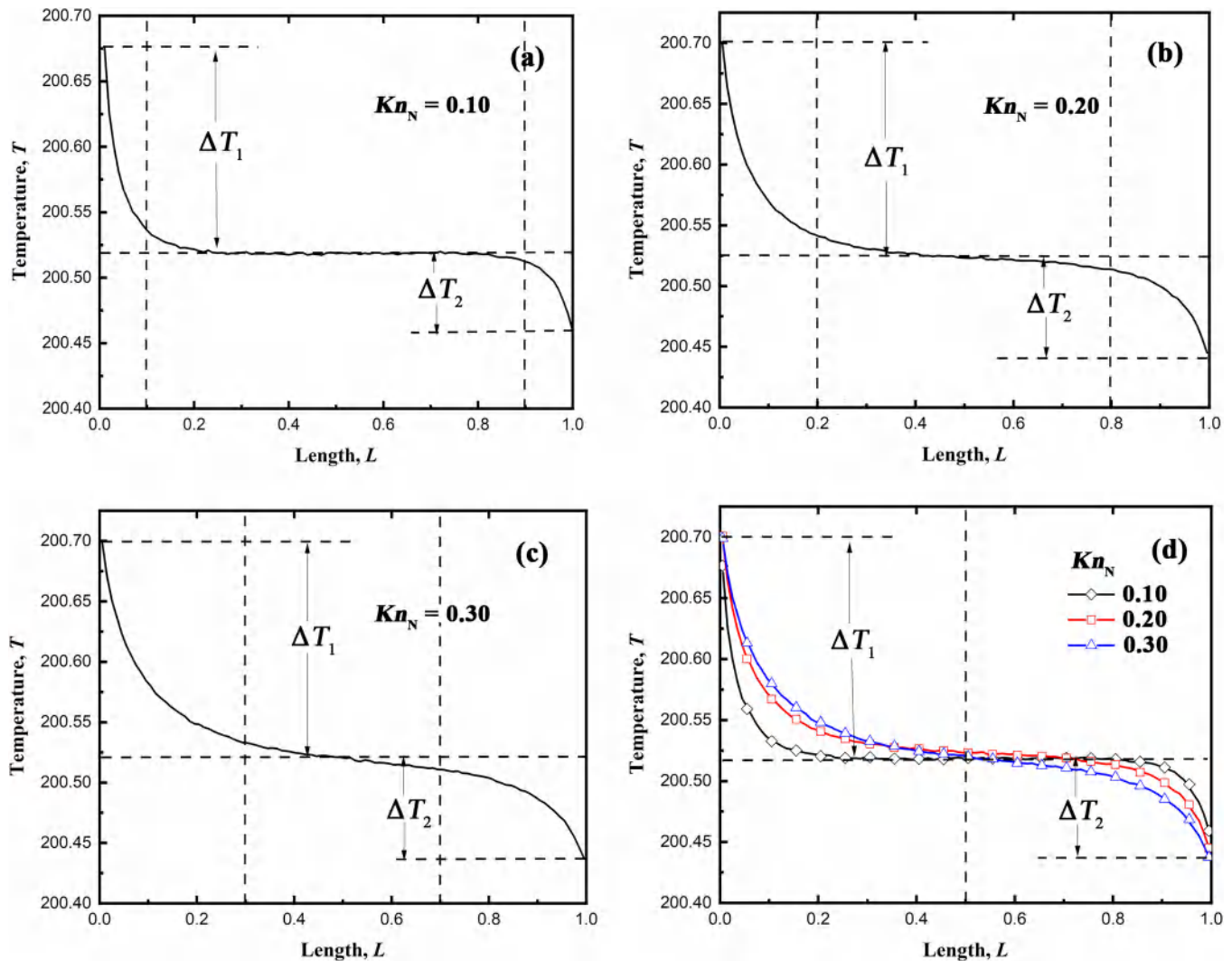


**FIG. 6.** When the heat flux boundary is adopted, the steady temperature profile is depicted for the nanofilms with finite length in phonon hydrodynamics at different mean free paths, (a)  $\lambda_N = 500$  nm, (b)  $\lambda_N = 1000$  nm, and (c)  $\lambda_N = 1500$  nm. (d) is the combination of the previous three figures.

Einstein distribution. When phonons are scattered, the steady distribution changes from non-collective distribution to collective one. Therefore, the phonons that propagate from the right to the left at  $x = 0.01$  follow the collective distribution. Considering these characteristics, the left and the right parts in phonon direction distribution might have different drift velocities individually, which is denoted as  $\mathbf{u}_{\text{left}}$  and  $\mathbf{u}_{\text{right}}$ , respectively. Then drift velocity distributions are plotted in Fig. 8.

In Fig. 8, as discussed before,  $\mathbf{u}_{\text{right}}$  at  $x = 0.0$  is zero and  $\mathbf{u}_{\text{left}}$  at  $x = 1.0$  is also zero. As for  $\mathbf{u}_{\text{right}}$ , with the increasing of  $x$ , the drift velocity gradually increases and becomes nearly constant at last. When  $x$  approaches 1.0, the drift velocity slightly rises. Similar principles are also satisfied for  $\mathbf{u}_{\text{left}}$ . This kind of representation is

inconvenient. They are only used to explain the transition process from non-collective to collective. Two kinds of revised drift velocities are analyzed.

The first kind of drift velocity  $\mathbf{u}_1$  is defined based on the weighted average of  $\mathbf{u}_{\text{left}}$  and  $\mathbf{u}_{\text{right}}$

$$\mathbf{u}_1 = p_{\text{left}}\mathbf{u}_{\text{left}} + p_{\text{right}}\mathbf{u}_{\text{right}}. \quad (18)$$

$p_{\text{left}}$  and  $p_{\text{right}}$  are the proportions of the phonon energy of the left part and the right part in the entire energy regime, respectively. In the second way, the drift velocity can be defined directly as the

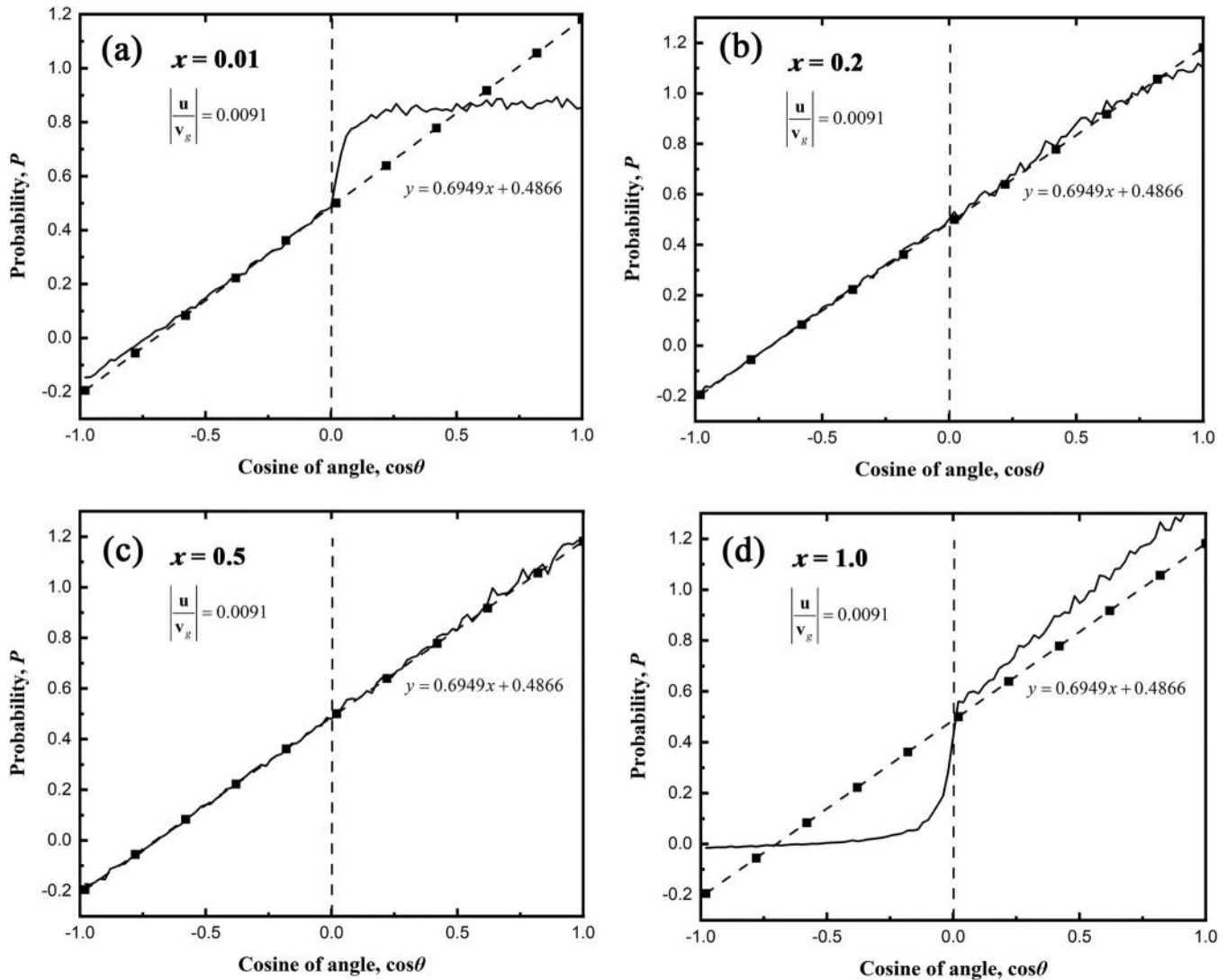


FIG. 7. The probability distribution function of the phonon velocity directions along with polar angle  $\theta$  at different positions, (a)  $x = 0.01$ , (b)  $x = 0.2$ , (c)  $x = 0.5$ , and (d)  $x = 1.0$ .

average of  $u_{left}$  and  $u_{right}$

$$\mathbf{u}_2 = \frac{\mathbf{u}_{left} + \mathbf{u}_{right}}{2}, \tag{19}$$

denoted as  $\mathbf{u}_2$ . These distributions are plotted in Fig. 9(a), which agree with Lee’s results.<sup>29</sup> It can be found that  $\mathbf{u}_1$  is approximately equal to  $\mathbf{u}_2$  due to the small drift velocity. Therefore, this article used  $\mathbf{u}_1$  to represent the total drift velocity  $\mathbf{u}_d$ . The drift velocity has a nonzero value at the boundary and the maximum value appears in the middle part. The drift velocity ratio distributions with different Knudsen numbers are plotted in Fig. 9(b). Their

profile shapes are similar. The maximum ratios at different Knudsen numbers are the same. However, when  $Kn$  is lower, the boundary velocity ratio climbs faster to the maximum and goes down later, corresponding to the higher scattering rate. In addition, at the boundary, the higher  $Kn$  corresponds to the lower velocity ratio.

Following the method adopted by Lee,<sup>29</sup> the entropy production caused by the N process can be calculated by

$$\dot{S}_{scatt} = \frac{1}{TNV} \int \int_{V,K} \varphi(\mathbf{K}, x) \dot{f}_{scatt}(\mathbf{K}, x) dV d\mathbf{K}, \tag{20}$$

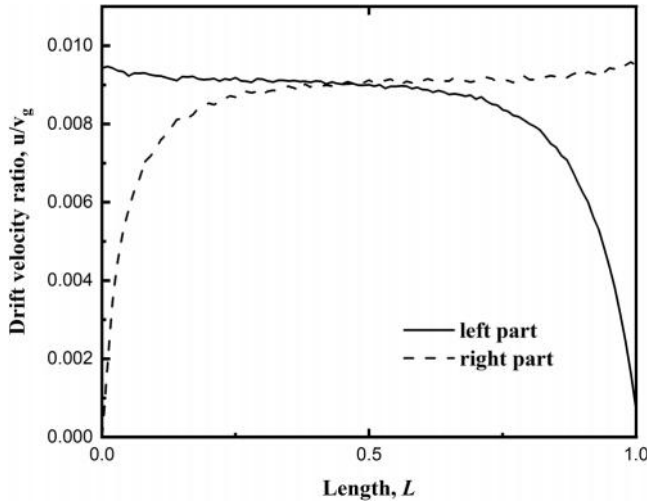


FIG. 8. Individual drift velocity of the left part  $u_{\text{left}}$  and right part  $u_{\text{right}}$  of the velocity direction distribution.

where  $N$ ,  $V$ , and  $T$  represent the number of phonon states, the volume, and the temperature, respectively.  $\varphi$ , which has the dimension of energy, is defined by the deviation between the real phonon distribution  $f$  and the equilibrium Bose–Einstein distribution  $f_0$  as

$$f(\mathbf{K}, x) = f_0 - \varphi \frac{\partial f_0}{\partial (\hbar\omega)}. \quad (21)$$

According to Lee,<sup>29</sup> the entropy production is related to thermal resistance as

$$R = \frac{T^2 \dot{S}}{\dot{Q}^2}. \quad (22)$$

In phonon hydrodynamics, the equilibrium state becomes the displaced Bose–Einstein distribution. The relaxation time approximation method is then adopted to depict the time evolution of phonon scattering distribution when the resistance scattering process is ignored, as

$$\dot{f}_{\text{scatter}} = \frac{f - f_d}{\tau_N}. \quad (23)$$

The phonon distribution can be divided into two parts, according to the principles in Fig. 7, namely, the positive part  $f_+$  denoting the phonons that propagate along with  $x$  coordinate and the negative part  $f_-$  denoting the phonons in the opposite direction.

Therefore, Eq. (23) can be rewritten as

$$\dot{f}_{\text{scatter}} = \frac{(f_+ - f_{d+}) + (f_- - f_{d-})}{\tau_N}. \quad (24)$$

Then, the entropy production can be obtained by substituting Eq. (24) into Eq. (20),

$$\begin{aligned} \dot{S}_{\text{scatt}} = & \frac{1}{TNV\tau_N} \left[ \int_{V, \mathbf{K}^+} \phi(\mathbf{K}, x)(f_+ - f_{d+}) dV d\mathbf{K} \right. \\ & \left. + \int_{V, \mathbf{K}^-} \phi(\mathbf{K}, x)(f_- - f_{d-}) dV d\mathbf{K} \right]. \quad (25) \end{aligned}$$

Entropy production arises in phonon transition from non-collective to collective, as shown in Eq. (25). If  $f_+ = f_{d+}$  and  $f_- = f_{d-}$ , no thermal resistance will be produced. On the contrary, if the original phonon distribution does not follow the displaced Bose–Einstein distribution, thermal resistance is produced. The boundary scatters and emits the phonons based on the equilibrium Bose–Einstein distribution, and after the redistribution of the normal scattering process, the phonon distribution approaches the displaced one. As plotted in Fig. 7, the phonon distributions in the steady hydrodynamic heat conduction at different positions do not totally satisfy the displaced Bose–Einstein distribution. Therefore, the hydrodynamic thermal resistance is attributed to the boundary effect. In the middle part of the media, the phonon distribution keeps unchanged, as shown in Fig. 7(c), thus producing no thermal resistance.

Apart from the aspect of velocity direction distribution, the thermal resistance in the phonon hydrodynamic regime can be understood in other ways. From the view of particle propagation, phonons are emitted from the boundary into the inner, and if none of them are scattered, all the phonons would arrive at the opposite boundary without any loss, which belongs to the ballistic heat transport. However, when the scattering process occurs, some phonons turn back to the original boundary and the others continue to propagate forward. These phonons that turn back lead to the heat flux reduction in phonon hydrodynamic heat conduction and generate the thermal resistance. It ought to be noticed that phonons come from both the high temperature and the low temperature, but the higher temperature boundary has more backflow phonons than the lower temperature boundary, resulting in the net backflow heat flux to the high temperature boundary.

When the length of the regime  $L$  is large enough, the heat flux and boundary temperature difference do not change with length anymore, causing invariant thermal resistance. Thus, the thermal conductivity  $k$ , which is related to thermal resistance  $R$  as  $k = L/R$  in phonon Poiseuille hydrodynamic heat conduction might be length dependent. Here, two kinds of thermal conductivity are analyzed, namely, the hydrodynamic thermal conductivity and the effective thermal resistance. At the same time, two kinds of thermal resistance are named as hydrodynamic thermal resistance and effective thermal resistance. Here, the high- and low-temperature boundaries are set as  $T_1$  and  $T_2$ , and the temperatures of the left

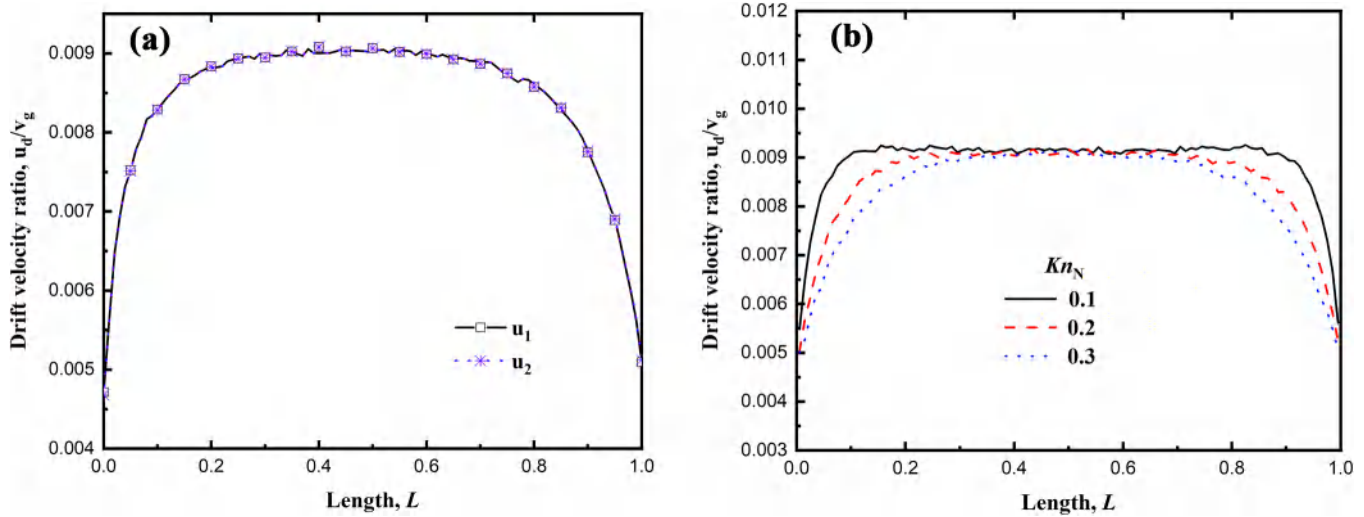


FIG. 9. (a) The two kinds of drift velocity distributions  $u_1$  and  $u_2$  along with the length. (b) The drift velocity distributions along with the length at different Knudsen numbers.

and the right sides for this regime are  $T_{left}$  and  $T_{right}$ , respectively. It is known that  $T_1 > T_{left}$  and  $T_2 < T_{right}$ . The heat flux is  $q$  and the nanofilm length is  $L$ . Due to phonon distribution transition from the equilibrium Bose–Einstein distribution to the displaced one, boundary temperature step differences exist, such as  $\Delta T_1$  and  $\Delta T_2$ . Therefore, the hydrodynamic thermal conductivity is defined as

$$k_h = \frac{qL}{(T_{left} - T_{right})}, \quad (26)$$

and the effective thermal conductivity is expressed as

$$k_e = \frac{qL}{(T_1 - T_2)}. \quad (27)$$

Another way to represent the thermal behaviors at the boundary is to adopt the thermal resistance. The effective thermal resistance is defined similar to the effective thermal conductivity,

$$R_e = \frac{(T_1 - T_2)}{q}, \quad (28)$$

while the hydrodynamic thermal resistance is

$$R_h = \frac{(T_{left} - T_{right})}{q}. \quad (29)$$

The effective thermal resistance can be regarded to consist of two boundary resistances and one hydrodynamic thermal

resistance,

$$\begin{aligned} R_e &= R_{left} + R_{right} + R_h \\ &= \frac{T_1 - T_{left}}{q} + \frac{T_{left} - T_{right}}{q} + \frac{T_{right} - T_2}{q} = \frac{T_1 - T_2}{q}. \end{aligned} \quad (30)$$

The hydrodynamic thermal resistance and the effective thermal resistance in phonon hydrodynamics are calculated in the range from  $Kn_N = 0.1$  to  $Kn_N = 1.6$ . The hydrodynamic thermal conductivity is higher than the effective thermal conductivity. The MFP of the N process is changed so that different Knudsen numbers are obtained. It reads from Fig. 10(a) that the hydrodynamic thermal conductivity decreases when  $Kn < 0.5$  and then increases with the growth of MFP. When  $Kn$  is small, the mean free path has few influences on the heat flux, but the increment of MFP leads to a larger boundary temperature step difference. When the Knudsen number is large, ballistic heat transport plays a non-negligible role in heat conduction. More ballistic phonons appear as the MFP increases. In the other way around, the effective thermal conductivity increases when  $Kn$  goes up, although the effective thermal conductivity varies in a small range.

### C. Thermal resistance in Ziman hydrodynamic heat conduction

When the characteristic length of the regime and the MFPs satisfy the relation,  $\lambda_N < \lambda_R < L$ , heat transport will fall into the Ziman hydrodynamic regime, where the resistance scattering process also influences the heat flux and temperature. A one-dimensional heat conduction problem is considered, whose schematic diagram is plotted in Fig. 2(a). The coupling effects are compared with those cases where the N process is ignored, as shown in Fig. 11. When the N process is ignorable, it belongs to the ballistic-

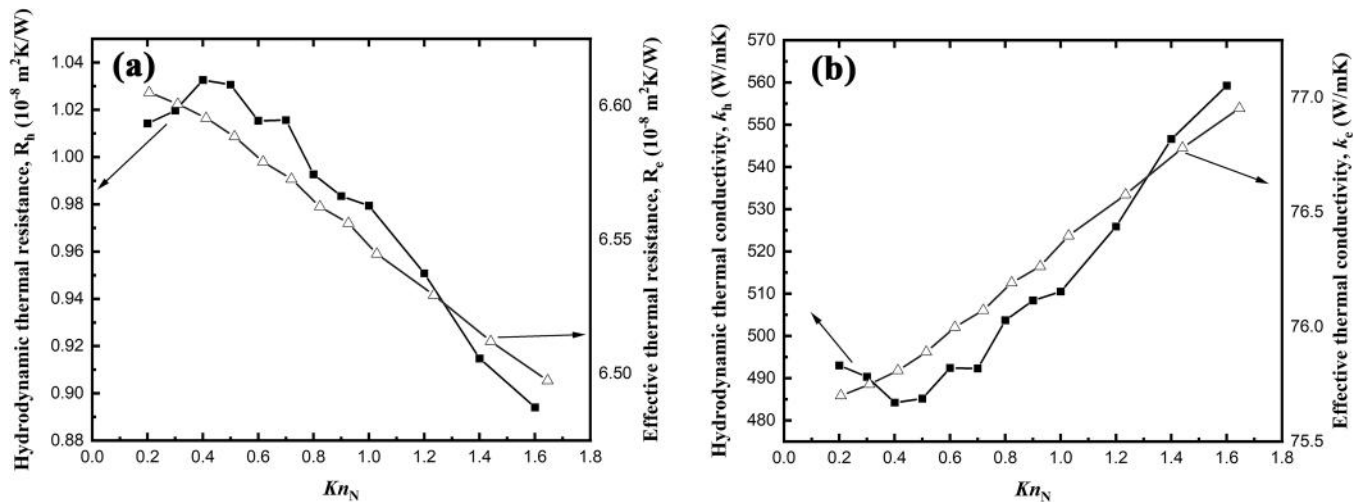


FIG. 10. (a) Hydrodynamic thermal resistance and effective thermal resistance of the given material with finite length at different Knudsen numbers. (b) Hydrodynamic thermal conductivity and effective thermal resistance of the given material with finite length at different Knudsen numbers.

diffusive regime. The temperature profile is linear along with the length. In the Ziman hydrodynamic regime,  $Kn_N$  and  $Kn_U$  are defined as the ratio of MFP of the N process and the U process with respect to the characteristic length, respectively, as Eqs. (15) and (16). The boundary temperature step can be found at the two boundaries of the nanofilm. In the middle part, the temperature distribution is linear, similar to that predicted by diffusive heat conduction. As for the heat flux distribution profile, the N process increases the proportion of phonons that are reflected to the boundary, decreasing the total heat flux.

In Fig. 12, the regime length is set to be 5000 nm and the mean free path of the N process is 500 nm. The MFPs of the U process vary from 500 to 8000 nm, falling from the ballistic-diffusive regime to the phonon hydrodynamic regime. The temperature profile is linear when  $\lambda_U$  is short, and it becomes curved with the increase in  $\lambda_U$ . When the MFP of the U process is comparable to that of the N process, the U process dominates the heat conduction and the N process is covered up. The existence of the U process brings thermal resistance to the heat transport and leads to a temperature gradient. The patterns in Figs. 11 and 12 resemble the analytical predictions by Hua and Minnich.<sup>63</sup>

The influences of the N process can be observed from the comparisons of the temperature profiles and the thermal conductivity between the pure U process and the coupling process of N and U, as shown in Figs. 11 and 13. When  $\lambda_U$  is comparable to  $\lambda_N$  ( $Kn = 0.1$ ), these two temperature profiles are much similar and the U process dominates the whole scattering process. As  $\lambda_U$  increases, they separate with nearly the same high temperature  $T_{\text{left}}$  and different low temperatures  $T_{\text{right}}$ . It is found that the coupling process has a smaller temperature difference  $\Delta T$  ( $\Delta T = T_{\text{left}} - T_{\text{right}}$ ). The hydrodynamic thermal conductivity and the effective thermal conductivity are analyzed here, and it is found that the coupling process has higher thermal conductivity. It implies that the N

process can enhance thermal conductivity. It is demonstrated that the displaced Bose-Einstein distribution leads to direction-preferable phonon wave vector distribution, which could decrease the backward phonons and enhance the heat flux. Therefore, the N process increases the thermal conductivity, both the hydrodynamic thermal conductivity and the effective thermal conductivity, as plotted in Fig. 13.

#### D. Hydrodynamic interfacial resistance

The interfacial effects on thermal resistance are complex as demonstrated by Frank.<sup>62</sup> Here, the interface transmissivity  $t$  and specular reflectivity  $s$  are adopted to describe the interfacial interactions. When phonons meet the interface, some are reflected and the others pass through the interface. The calculation schematic diagram is plotted in Fig. 2(b). When the interface transmissivity  $t$  is equal to 1 and the specular reflectivity  $s = 0$ , the steady temperature distribution profiles are shown in Fig. 14.

In both the nanofilms, the boundary temperature steps appear in the typical hydrodynamic temperature profiles. Also, in Fig. 14(a) at the interface, although the heat flux flows from left to right, the temperature difference at the interface is positive. That is to say, heat transports from lower temperature to higher temperature. It is impossible in the framework of Fourier's law. However, it is the hydrodynamic heat conduction and the conventional definition of temperature that fails. Thus, the value of temperature is a measurement of local energy density. In the following research studies, it is found that the inverse temperature gradient gradually disappears with increasing specular reflectivity,  $s$ . When  $s = 1.0$ , all the phonons follow Fresnel's law. In this case, when the two nanofilms are made of the same material, phonons keep their original frequency and direction so that the interface disappears. The temperature difference between the two nanofilms at the interface is called interfacial temperature difference.

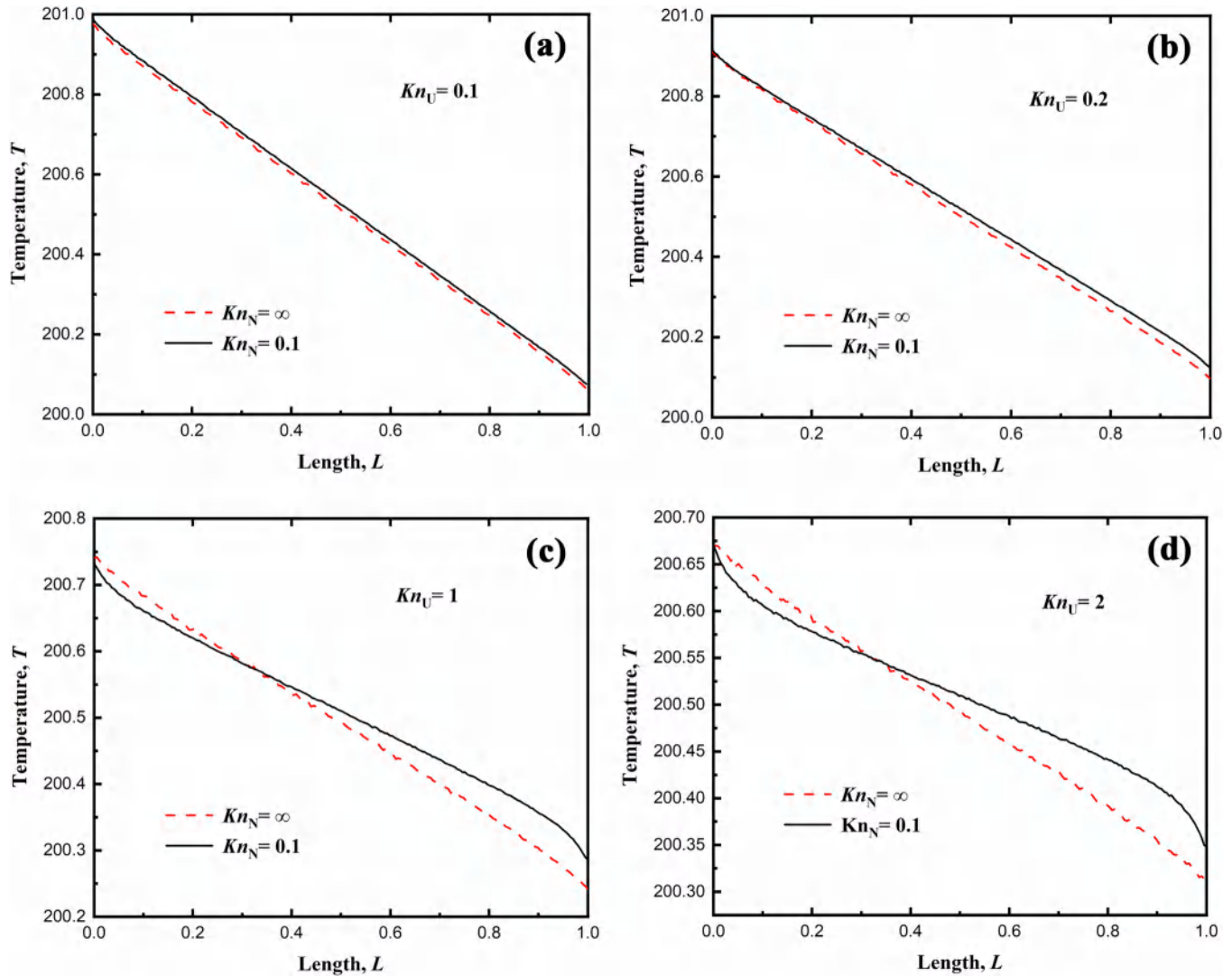


**FIG. 11.** Comparisons of the temperature profiles in the nanofilms between ballistic-diffusive and Ziman hydrodynamic heat transport at different Knudsen numbers of the U process. (a)  $Kn_U = 0.1$ , (b)  $Kn_U = 0.2$ , (c)  $Kn_U = 1.0$ , and (d)  $Kn_U = 2.0$ .

When the interface transmissivity  $t$  changes from 1.0 to 0.0, the proportion of phonons that can pass through the interface goes down.  $t = 0.0$  means that no phonons could get through the interface, implying that the boundary is adiabatic. In addition, the temperature differences at both sides of the interface are plotted in Fig. 15, which shows that when the interface transmissivity  $t$  increases, the temperature difference goes down linearly. The energy density in the left nanofilm changes a little while that in the right nanofilm grows with the increasing interface transmissivity  $t$ , resulting in the change of interface temperature difference.

Boundary specular reflectivity is also an important parameter in interfacial thermal resistance. When  $s = 0$ , all the phonons are redistributed based on equilibrium Bose–Einstein distribution for

frequency and Lambert distribution for velocity. When  $s = 1.0$ , all the phonons keep their original properties. With constant transmissivity  $t$ , the change of  $s$  mainly influences the profile shape, as shown in Fig. 16, where the two figures have transmissivity  $t = 0.1$  and  $t = 0.5$ , respectively and the specular reflectivity  $s$  varies from 0.1 to 0.9. The interface temperature difference goes up as the specular reflectivity increases and, finally, reaches zero at  $s = 1.0$ . At the same time,  $s$  also influences the steady state energy density at both nanofilms. When  $s$  goes up, the energy densities in both nanofilms increase, and the left part is influenced more, just the other way around with respect to interface transmissivity  $t$ . The energy difference at the interface grows as well when  $s$  goes up. This tendency is compatible with the tendency of temperature difference at the interface.

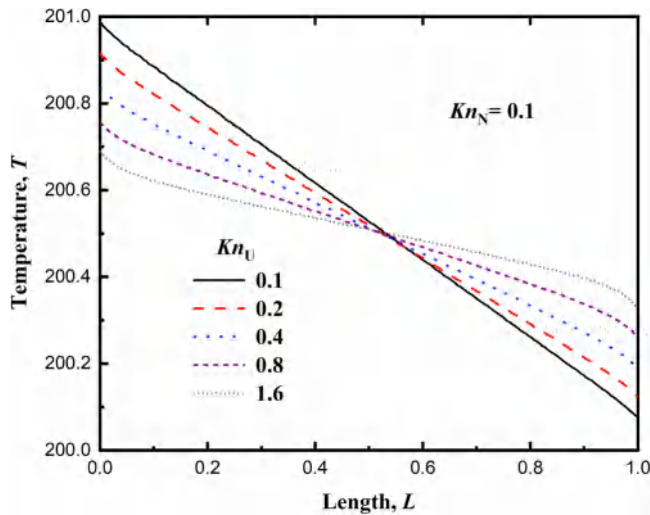


**FIG. 12.** Steady temperature profiles in the Ziman hydrodynamic regime with different  $\lambda_U$  and the same  $\lambda_N = 500$  nm. The whole length is 5000 nm and normalized to 1.

Figure 17 shows the variance of temperature differences at the interface along with specular reflectivity  $s$  at different interface transmissivity  $t$ ,  $t = 0.1, 0.3, 0.5, 0.7,$  and  $0.9$ . The discrete points represent the MC simulations and the solid lines denote the fitting functions. It is found that with increasing specular reflectivity, the temperature differences increase linearly. When  $s$  approaches 1, the temperature difference arrives at the maximum. In addition, the reduction in transmissivity results in higher temperature difference, as fewer phonons can get through the interface and larger thermal resistance is produced. The data points are fitted in linear lines, the expressions of which are also denoted in Fig. 17.

The interfacial thermal resistance at these cases  $R_i$  is calculated as

$$R_i = \frac{q}{(T_+ - T_-)}, \quad (31)$$

where  $T_+$  and  $T_-$  represent the temperature of the right and left sides at the interface, respectively. The principles for the thermal resistance and thermal conductivity along with phonon interface transmissivity and specular reflectivity are plotted in Fig. 18(a). Different shapes of the points represent different interface transmissivities. With the increasing specular reflectivity, thermal resistance increases as well and approaches a constant value. When specular reflectivity  $s$  is larger than 0.6, thermal resistance nearly keeps constant. When the transmissivity  $t = 0.1$ , the thermal resistance increases at first and then decreases, which is because specular reflectivity has larger influences on interface temperature difference at  $t = 0.1$ . In addition, this figure also reveals the relation between transmissivity and thermal resistance. Larger transmissivity  $t$  leads to lower thermal resistance corresponding to the difficulty of phonons passing through the interface.

Since temperature is ill-defined in phonon hydrodynamics, it is not proper to discuss the interfacial thermal resistance in conventional definition. Thus, effective thermal conductivity is analyzed as calculated by

$$k_{ei} = \frac{qL}{(T_1 - T_2)}. \quad (32)$$

The combined structure includes two nanofilms with finite length and infinite width, as shown in Fig. 2(b). The resistance consists of two boundary resistances (left and right boundary) and one interfacial thermal resistance, and they are plotted in Fig. 18(b). The length of each nanofilm is 2500 nm as the total regime length is 5000 nm. It is obvious that high interface transmissivity causes a larger heat flux and enhances the thermal conductivity. Specular reflectivity also influences the thermal conductivity slightly, which increases with  $s$  going up. The specular reflectivity  $s$  reflects the ability of the interfacial phonons to conserve their momentum. When the specular reflectivity  $s$  is higher, less phonon momentum is destroyed, thus enhancing heat transport.

The existence of the interface not only increases the backward phonons, but also influences the thermal conductivity by the interactions with phonons, such as in the way of interface transmissivity  $t$  and specular reflectivity  $s$ .

#### IV. THEORETICAL MODELS

In this section, two theoretical models are proposed to depict the temperature distribution in steady heat conduction in phonon hydrodynamics. They are the particle propagation model and the dual boundary flux model. In the particle propagation model, the particles are scattered and counted in simpler principles, and it gives a clear explanation for the heat flux reduction phenomenon. Moreover, the dual boundary flux model classifies the heat flux into two categories—the hydrodynamic heat flux and the diffusive heat flux. It gets better accuracy for temperature distribution in the steady heat conduction process. Then, the predictions of these two models are compared in Sec. IV C. The interfacial temperature difference and interfacial thermal resistance are depicted by the dual boundary flux model in Sec. IV D.

##### A. Particle propagation model

The particle propagation model traces the emitting and scattering processes of the phonon particles from the boundary and gives these phonons simpler scattering rules.<sup>75</sup> This model can be used to explain the phenomenon of heat flux reduction in hydrodynamic heat conduction. There are three assumptions for the particle propagation model. (M1.1) The lifetime of each phonon is assumed to be constant. Different phonons are supposed to have different lifetimes, but when their lifetimes are set to be equal, they will travel the same distance before being scattered. In other words, if all the phonons are scattered at the same time, then the next time, they would be scattered at the same time, as well. (M1.2) The drift velocity  $\mathbf{u}_d$  along with the whole nanofilm is regarded to be the same. This assumption has some problems near the boundary, as demonstrated in Sec. IV A. Nevertheless, here it is used to have a quality understanding of the temperature profile distributions.

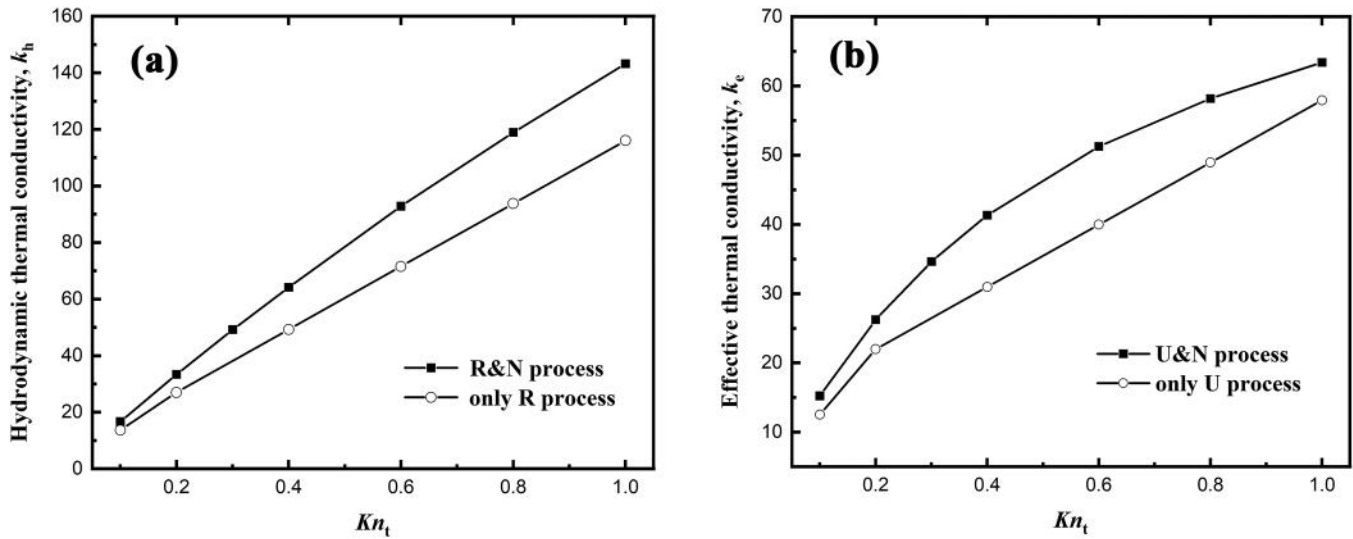


FIG. 13. The distribution of hydrodynamic thermal conductivity (a) and effective thermal conductivity (b) of the given material with different Knudsen numbers in Ziman hydrodynamic heat transport and diffusive heat transport.

(M1.3) To make the expression simpler, the Debye model is assumed and the following approximation is adopted:

$$E_0 = \int_0^{\omega_D} f_0(\omega) D(\omega) \hbar \omega d\omega \approx \frac{1}{4} \int_0^{\omega_D} f_0(f_0 + 1) \frac{\hbar \omega}{kT_0} D(\omega) \hbar \omega d\omega. \quad (33)$$

This equation is correct when temperature  $T_0$  is much lower than Debye temperature  $T_D$ .

Temperature and adiabatic boundary conditions are considered individually. Temperature boundary absorbs all the phonons that arrive at the boundary and re-emits the phonons according to the given temperature in equilibrium Bose–Einstein distribution. Adiabatic boundary reflects all the phonons coming back and keeps their frequency. If there is no resistance, all the phonons emitting from the high temperature boundary can arrive at the low temperature boundary so can the phonons from the low temperature boundary. However, when the phonons are scattered inside the

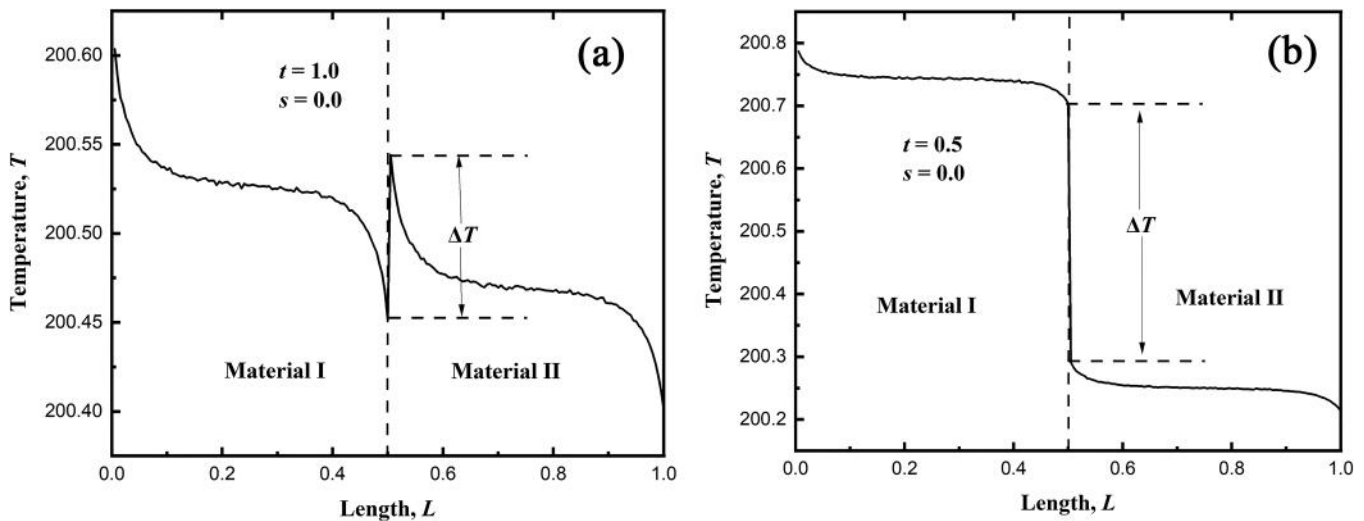
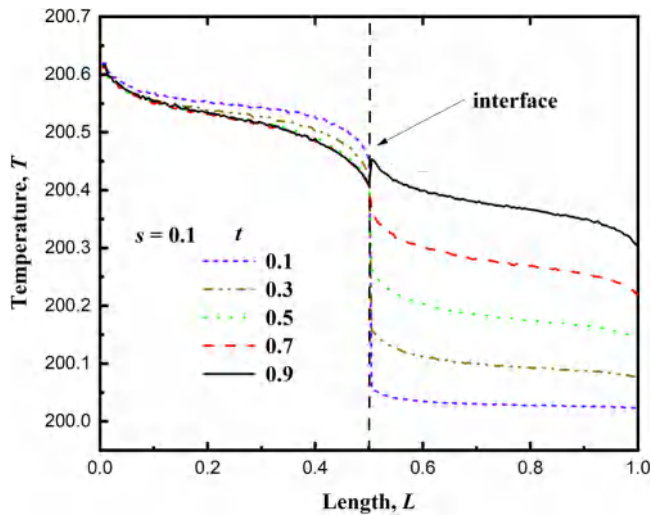


FIG. 14. Steady temperature distribution profiles in Poiseuille hydrodynamic heat conduction when (a)  $t = 1.0$  and  $s = 0.0$  and (b)  $t = 0.5$  and  $s = 0.0$ .



**FIG. 15.** The steady temperature profile in Poiseuille hydrodynamic heat conduction when  $s = 0.1$  at different transmissivity values  $t = 0.1, 0.3, 0.5, 0.7,$  and  $0.9$ .

media, some phonons have been reflected to their original boundary and then absorbed. Since the high temperature end has more emitting phonons than the low temperature end, more phonons go back to the high temperature end than the low temperature end. Thus, the heat flux propagating from high temperature to low temperature is reduced by these reflected phonons.

New scattering rules are given to these phonons. Based on the assumption (M1.1), all the phonons can travel a constant length  $\lambda_N$

before they are scattered. In this way, in the given finite volume, the total phonon number is proportional to the phonons that are scattered during a given time interval, and their relationship is expressed as

$$r_s(\omega) = P_\lambda f(\omega), \tag{34}$$

where  $r_s$ ,  $P_\lambda$ , and  $f$  are the phonon scattering distribution function, phonon scattering possibility function, and phonon density function, respectively. Figure 19 shows the schematic of the particle propagation model at temperature boundary, where the heat flux propagates from the left to the right and  $T_1 > T_2$ . Points 1, 2, and 3 are the center of the circle, and the radius of the circle is  $\lambda_N$ . The rod is assumed to be isotropic and has a finite length and infinite width.

As mentioned before, if the direction of the drift velocity is assumed to be along with  $x$  coordinate and the phonon drift velocity is much smaller than their group velocity, the displaced Bose-Einstein distribution  $f_d$  is linearized as

$$f_d^{\text{linear}}(\omega, \mathbf{u}_d) = f_0 + \frac{\hbar}{k_B T} f_0 (f_0 + 1) \mathbf{K} \cdot \mathbf{u}_d. \tag{35}$$

$\mathbf{K}$  and  $\mathbf{u}_d$  are the phonon wave vector and phonon drift velocity, respectively. Then, the polar angle  $\theta$  distribution is

$$f_d^{\text{angle}}(\theta) = f_0 \sin \theta + \frac{\hbar}{k_B T} f_0 (f_0 + 1) K u_d \cos \theta \sin \theta, \tag{36}$$

where polar angle  $\theta$  is defined as the angle between the phonon velocity vector and  $x$  coordinate and  $f^{\text{angle}}$  is the angle distribution function of these phonons.

First, the temperature profile at the left boundary (high temperature boundary) is analyzed. The phonons propagate forward,

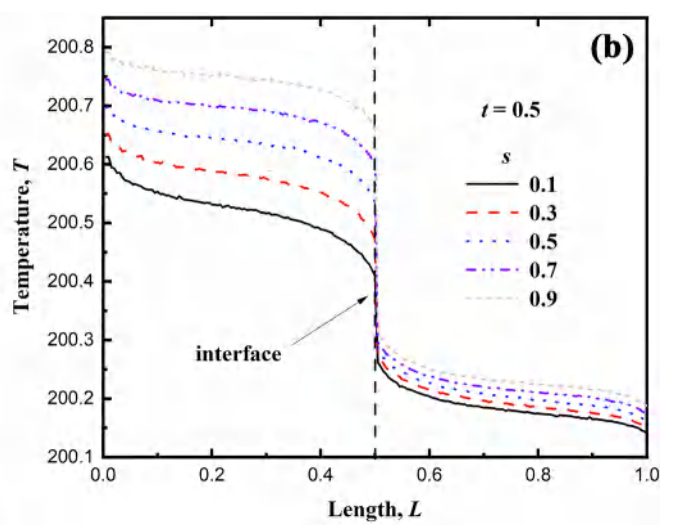
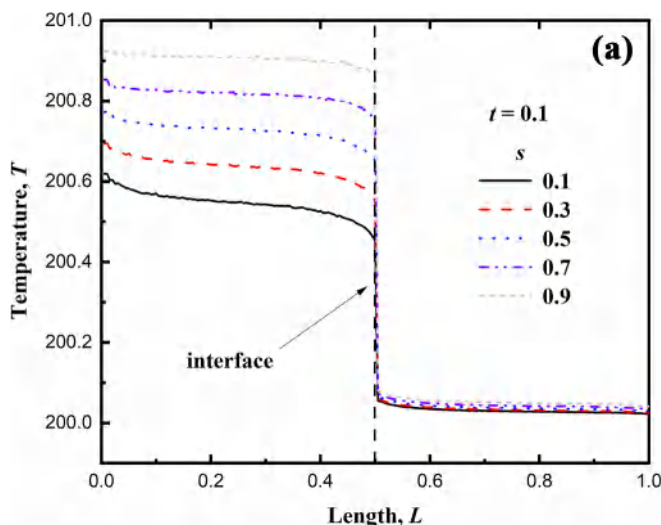


**FIG. 16.** Steady temperature profiles in Poiseuille hydrodynamic heat conduction at different specular reflectivity values  $s = 0.1, 0.3, 0.5, 0.7,$  and  $0.9$  when (a)  $t = 0.1$  and (b)  $t = 0.5$ .

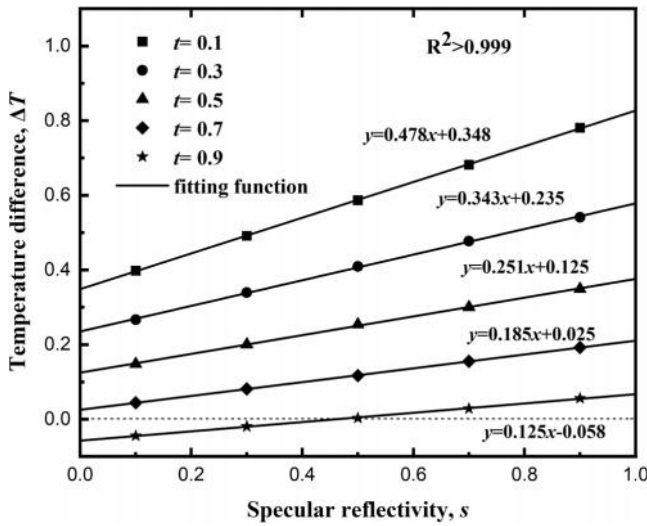


FIG. 17. Temperature differences between the interface at different specular reflectivities  $s$  and interface transmissivity  $t$ . The solid lines are the fitting functions of the discrete points.

and then, they are scattered to redistribute their directions, leading some phonons to go back. These phonons are absorbed by the absorbing boundary, resulting in heat flux reduction. If all the phonons starting from the boundary have been scattered, the percent of phonons that turn back is constant, so that the heat flux reduction does not depend on the regime length and the phonon mean free path. Now, the thermal energy densities at points 1, 2, and 3 are analyzed. Point 1, in the middle of the rod, can receive the phonon scatterings from all directions. Thus, the total number of phonons that are scattered at point 1 in the given time interval has been counted around the whole circle, as shown in Fig. 19. Since the travelling length of every phonon is constant, only the phonons at the circle around point 1 (as shown in Fig. 19) can be scattered. According to the first assumption, the phonon scattering rate is proportional to the local thermal energy density. Point 1 owns the whole circle. However, as for point 2, which is near the left boundary and satisfies  $x < l$ , not the whole perimeter of the circle contributes to point 2, considering the arc in an imaginary line. The critical angle of the circle area that can contribute to the given position  $x_2$  ( $x_2 < \lambda_{ave}$ ,  $\lambda_{ave}$  is the phonon travelling length which is constant) is

$$\theta_{c,2} = \arccos\left(\frac{x_2}{\lambda_N}\right). \quad (37)$$

The arc in the imaginary line is beyond the temperature boundary, which contributes to point 2 with equilibrium Bose–Einstein distribution and given boundary temperature. The energy density distribution in the regime is denoted as  $E(x)$ . According to the particle propagation principle, the energy density at point 2,  $E(x)$ ,

consists of the contribution from the circle area, which is

$$\begin{aligned} E(x) = & \frac{1}{2} \int_0^{\omega_D} d\omega \int_0^{2\pi} d\beta \int_{\frac{\pi}{2}}^{\pi} f \sin \theta D(\omega) d\theta \\ & + \frac{1}{2} \int_0^{\omega_D} d\omega \int_0^{2\pi} d\beta \int_{\frac{\pi}{2}}^{\pi} f(f+1) \frac{\hbar K}{kT} u_d \cos \theta \sin \theta D(\omega) d\theta \\ & + \frac{1}{2} \int_0^{\omega_D} d\omega \int_0^{2\pi} d\beta \int_{\theta_{c,2}}^{\frac{\pi}{2}} f_{left} \sin \theta d\theta. \end{aligned} \quad (38)$$

The integration with respect to  $\beta$  and  $\omega$  is done first, and Eq. (38) is transformed into

$$\begin{aligned} E(x) = & \frac{1}{2} \int_{\frac{\pi}{2}}^{\pi} \left[ E_{x+\lambda_N \cos \theta} \sin \theta + 4E_{x+\lambda_N \cos \theta} \frac{u_d}{v_g} \cos \theta \sin \theta \right] d\theta \\ & + \frac{1}{2} \int_{\theta_{c,2}}^{\frac{\pi}{2}} E_{left} \sin \theta d\theta. \end{aligned} \quad (39)$$

$E_{left}$  and  $E_{x+\lambda_N \cos \theta}$  are the energy densities at the left (high) temperature boundary and at the points at the circle.  $E_0$  is the energy density in the middle of the hydrodynamic nanofilm. In phonon hydrodynamic heat transport, there is no temperature gradient in the nanofilm center. The consequence of  $E_{left}$ ,  $E_{right}$ , and  $E_0$  is

$$E_{left} > E_0 > E_{right}. \quad (40)$$

If we assume  $E_{x+\lambda_N \cos \theta}$  to be equal to  $E_0$ , then Eq. (39) is transformed into

$$\begin{aligned} E(x) = & \frac{1}{2} \left[ E_{left} + E_0 - (E_{left} - E_0) \frac{x}{\lambda_N} \right] \\ & + E_0 \frac{u_d}{v_g} \left[ \left( \frac{x}{\lambda_N} \right)^2 - 1 \right]. \end{aligned} \quad (41)$$

In this way, the temperature profile is depicted in a quadratic function. However, this model makes many assumptions and, thus, misses lots of details. It can only give qualitative predictions. When  $x = 0$ , point 2 is located at the left boundary, and the energy density is

$$E(x=0) = \frac{1}{2} (E_{left} + E_0) - E_0 \frac{u_d}{v_g}, \quad (42)$$

corresponding to the nonequilibrium temperature  $T(x=0)$ . The difference between  $T(x=0)$  and  $T_0$  ( $\Delta T = T(x=0) - T_0$ ) is just the so-called boundary temperature step. It can be found that at the high-temperature boundary, the temperature step decreases with higher drift velocity. When  $x = \lambda_N$ , the energy density is  $E_0$ , compatible with the middle area of the rod.

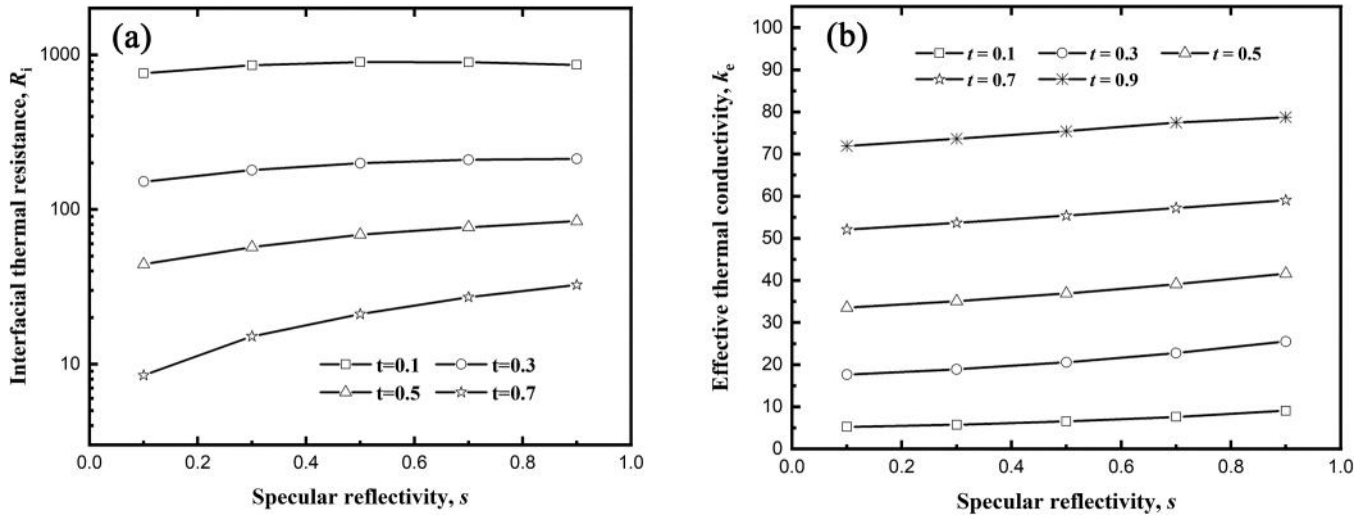


FIG. 18. Interfacial thermal resistance (a) and effective thermal conductivity (b) of the given material at different specular reflectivity  $s$  and interface transmissivity  $t$ .

In the same way, the energy density near the right boundary can also be written as

$$E(L - y) = \frac{1}{2} \int_0^{\theta_{c,3}} \left[ E_{L-y+\lambda_N \cos \theta} \sin \theta + 4E_{L-y+\lambda_N \cos \theta} \frac{u_d}{v_g} \cos \theta \sin \theta \right] d\theta + \frac{1}{2} \int_{\theta_{c,2}}^{\pi} E_{right} \sin \theta d\theta, \tag{43}$$

where  $y$  is the distance of point 3 from the right boundary. The

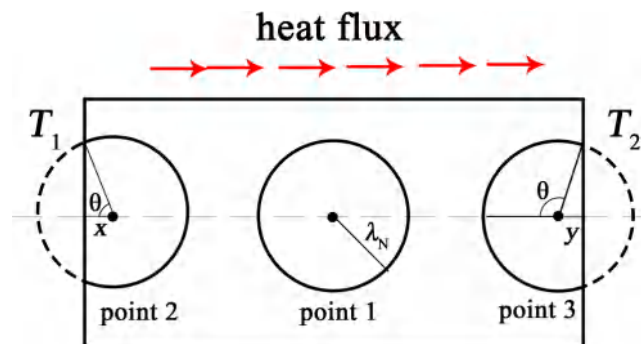


FIG. 19. Schematic diagram of the particle propagation model. The circle represents the areas that contribute to the given points.

critical angle  $\theta_{c,3}$  is

$$\theta_{c,3} = \arccos\left(-\frac{y}{\lambda_N}\right). \tag{44}$$

If the energy density  $E_{L-y+\lambda_N \cos \theta}$  is thought to be equal to  $E_0$ , this expression is simplified into

$$E(L - y) = \frac{1}{2} \left[ E_{right} + E_0 + (E_0 - E_{right}) \frac{y}{\lambda_N} \right] + E_0 \frac{u_d}{v_g} \left[ 1 - \left( \frac{y}{\lambda_N} \right)^2 \right]. \tag{45}$$

The boundary energy density  $E(L)$  is

$$E(L) = \frac{1}{2} (E_{right} + E_0) + E_0 \frac{u_d}{v_g}, \tag{46}$$

corresponding to temperature  $T(L)$ . If the middle energy density  $E_0$  is equal to the average value of  $E_{left}$  and  $E_{right}$ , which is thought to be approximately correct,

$$E_0 = \frac{(E_{left} + E_{right})}{2}, \tag{47}$$

the energy density differences at the boundary are equal,

$$E(0) - E_0 = E_0 - E(L). \tag{48}$$

The absolute values of boundary temperature steps at the two boundaries are also equal. This particle propagation model tries to explain hydrodynamic heat conduction resistance and the existence of the boundary temperature step.

The particle propagation model gives an easier way to understand the heat flux reduction in phonon hydrodynamic heat conduction and the origin of thermal resistance due to the interactions between phonon normal scattering and the boundary effect. If all the phonons emitted from the boundary can arrive at the other boundary without loss, which happens in the limit of ballistic phonon transport, there is no heat flux reduction. However, the phonon normal scattering process redistributes the phonon distributions and alters its direction. Therefore, some phonons are turned back to the original boundary, resulting in heat flux reduction.

### B. Dual boundary flux model

The second model is called the dual boundary flux model, and it recognizes that there are two kinds of phonon fluxes in the medium, similar to the classification from Sussmann.<sup>76</sup> The first one is the diffusive heat flux, where the phonons have no preferable directions, obeying the equilibrium Bose–Einstein distribution. The other is the hydrodynamic heat flux, where the phonon distribution obeys the displaced Bose–Einstein distribution. There are three assumptions in the dual boundary flux model. (M2.1) In the central part of the nanofilm, there is only the hydrodynamic heat flux. Nevertheless, at the boundary, only the diffusive heat flux is generated. (M2.2) When the thermal energy propagates in the medium from the boundary, the transition from the diffusive heat flux to the hydrodynamic heat flux appears at the assumed exponential rate. The transition corresponds to phonon distribution transition from the non-collective distribution to the collective one. (M2.3) The Debye model is adopted to make the expressions simpler.

In the steady state, where the system variables do not change with time anymore, the heat fluxes in the whole nanofilm are kept constant. It is assumed that the diffusion heat flux from the boundary has an exponential dissipative relation with distance, namely,

$$q_{diff} = q_0 \exp\left(-\frac{x}{\lambda}\right), \tag{49}$$

where  $q_0$  is the heat flux at the boundary. As the total heat flux does not change, the hydrodynamic heat flux increases,

$$q_{hydro} = q_0 - q_{diff} = q_0 \left[1 - \exp\left(-\frac{x}{\lambda}\right)\right]. \tag{50}$$

It can be understood in this way that the phonons from the boundary belong totally to the diffusive heat flux, and then, they are scattered and become one part of the hydrodynamic heat flux. Take the area near the left (high temperature) boundary, for example, according to the propagation directions, the phonons are divided into two parts according to the polar angle, namely,  $\cos \theta < 0$  and  $\cos \theta > 0$ , named as negative direction phonons and positive direction phonons. The phonons emitted from the left boundary are all positive direction phonons and those absorbed by the boundary are negative direction phonons. The positive direction phonons include both the diffusive flux and the hydrodynamic flux, which implies that the phonon distribution consists of both equilibrium Bose–

Einstein distribution and displaced Bose–Einstein distribution. At point 2, the negative direction phonons are the backward phonons that are scattered back. Therefore, they contribute to the hydrodynamic heat flux, which obeys the displaced Bose–Einstein distribution.

The phonons in different distributions result in different heat fluxes although the total thermal energy is equal. As the positive direction phonons, if these phonons are in the equilibrium Bose–Einstein distribution, the heat flux is

$$q_{diff} = \int_0^{\omega_D} d\omega \int_0^{2\pi} d\beta \int_0^{\frac{\pi}{2}} f_0(\omega, \theta, \beta) D(\omega) \hbar \omega v_g \cos \theta \sin \theta d\theta = \frac{1}{2} E_1 v_g. \tag{51}$$

where  $E_1$  represents the thermal energy, satisfying

$$E_1 = \int_0^{\omega_D} d\omega \int_0^{2\pi} d\beta \int_0^{\frac{\pi}{2}} f_0(\omega, \theta, \beta) D(\omega) \hbar \omega \sin \theta d\theta. \tag{52}$$

However, if these phonons follow the linearized displaced Bose–Einstein distribution, the heat flux is

$$q_{hydro} = \int_0^{\omega_D} d\omega \int_0^{2\pi} d\beta \int_0^{\frac{\pi}{2}} f_d^{linear}(\omega, \theta, \beta) D(\omega) \hbar \omega v_g \cos \theta \sin \theta d\theta = \frac{1}{2} E_1 v_g + \frac{1}{3} E_2 u_d, \tag{53}$$

where

$$E_2 = \int_0^{\omega_D} d\omega \int_0^{2\pi} d\beta \int_0^{\frac{\pi}{2}} f_0(1 + f_0) \frac{(\hbar \omega)^2}{k_B T} D(\omega) d\theta = 4\alpha E_1. \tag{54}$$

When Debye temperature  $T_D$  is much higher than  $T_0$ ,  $\alpha = 1$ . Otherwise,  $\alpha < 1$ , because  $E_2$  and  $u_d/v_g > 0$ ,  $q_{hydro} > q_{diff}$ . It is found that as for the positive direction phonons with the same thermal energy, the displaced Bose–Einstein distribution with positive drift velocity produces a higher heat flux than the equilibrium distribution. In other words, to produce the same heat flux, the diffusive heat flux in the equilibrium Bose–Einstein distribution requires higher energy density than the hydrodynamic heat flux in the displaced Bose–Einstein distribution,

$$q_0 = \frac{1}{2} E_{diff} v_g = \frac{1}{2} E_{hydro} v_g + \frac{4}{3} \alpha E_{hydro} u_d. \tag{55}$$

For the negative direction phonons, it is the other way around.

The thermal energy density ratio  $r_{E+}$  for phonons in the positive direction to produce the same heat flux is

$$r_{E+} = \frac{E_{diff}}{E_{hydro}} = 1 + \frac{8}{3}\alpha \frac{u_d}{v_g}. \quad (56)$$

The ratio for phonons in the negative direction  $r_{E-}$  is

$$r_{E-} = \frac{E_{diff}}{E_{hydro}} = 1 - \frac{8}{3}\alpha \frac{u_d}{v_g}. \quad (57)$$

In the area near the left (high temperature) boundary, the heat flux consists of the diffusive heat flux and the hydrodynamic heat flux,

$$\begin{aligned} q_0 &= q_{hydro} \\ &= q_{hydro|\cos\theta < 0} + q_{diff|\cos\theta > 0} \exp\left(-\frac{x}{\lambda}\right) \\ &\quad + q_{hydro|\cos\theta > 0} \left[1 - \exp\left(-\frac{x}{\lambda}\right)\right]. \end{aligned} \quad (58)$$

At the nanofilm middle, only the hydrodynamic heat flux exists. Therefore, the relationship between the phonon energy density near the left boundary  $E(x)$  and that in the central part  $E_0$  can be written as

$$\begin{aligned} E(x) &= \frac{E_0 - 2\alpha E_0 u_d / v_g}{2E_0} E_0 \\ &\quad + \frac{E_0 + 2\alpha E_0 u_d / v_g}{2E_0} E_0 \left[ \left(1 - e^{-\frac{x}{\lambda}}\right) + r_{E+} e^{-\frac{x}{\lambda}} \right]. \end{aligned} \quad (59)$$

Thus, the thermal energy difference is

$$\Delta E_{left} = E(x) - E_0 = \frac{4}{3}\alpha \frac{u_d}{v_g} \left(1 + 2\alpha \frac{u_d}{v_g}\right) e^{-\frac{x}{\lambda}} E_0. \quad (60)$$

The temperature difference or the boundary temperature step is proportional to the thermal energy difference. From Eq. (60), the temperature difference is related to the drift velocity and the steady energy density. Moreover, it is expressed in an exponential function.

At the right boundary, the positive direction phonons are in the displaced Bose–Einstein distribution, while the negative direction phonons are the mixture of the displaced Bose–Einstein distribution and the equilibrium Bose–Einstein distribution,

$$\begin{aligned} q_0 &= q_{hydro|\cos\theta > 0} + q_{diff|\cos\theta < 0} \exp\left(-\frac{y}{\lambda}\right) \\ &\quad + q_{hydro|\cos\theta < 0} \left[1 - \exp\left(-\frac{y}{\lambda}\right)\right]. \end{aligned} \quad (61)$$

The thermal energy near the right boundary  $E(L-y)$  is expressed in the form of  $E_0$ ,

$$\begin{aligned} E(L-y) &= \frac{E_0 + 2\alpha E_0 u_d / v_g}{2E_0} E_0 \\ &\quad + \frac{E_0 - 2\alpha E_0 u_d / v_g}{2E_0} E_0 \left[ \left(1 - e^{-\frac{y}{\lambda}}\right) + r_{E-} e^{-\frac{y}{\lambda}} \right]. \end{aligned} \quad (62)$$

Therefore, the energy density difference near the right boundary is negative,

$$\Delta E_{right} = E(L-y) - E_0 = -\frac{4}{3}\alpha \frac{u_d}{v_g} \left(1 + 2\alpha \frac{u_d}{v_g}\right) e^{-\frac{y}{\lambda}} E_0. \quad (63)$$

The dual boundary flux model focuses on the transition between the diffusive heat flux and the hydrodynamic heat flux and points out that the boundary temperature step appears near the boundary because these two fluxes have different energy densities. The boundary temperature step is important, no matter, for the thermal resistance or the temperature predictions in micro- and nano-structures. However, the assumed exponential transition rate cannot be verified rigorously because it regards that the ballistic phonons approach the equilibrium state only after scattering once.

### C. Comparisons between the theoretical model and simulations

The particle propagation model and the dual boundary flux model are proposed in Secs. IV B and IV C to study the boundary temperature step. However, since these models introduce some assumptions, fitting parameters are required to match the results. It is demonstrated that these theories depict the qualitative laws. To match the results, several fitting parameters are introduced to these two models, such as  $a$ ,  $b$ , and  $c$  in the following equations:

$$\begin{aligned} E(x) &= \frac{1}{2} \left[ E_{left} + E_0 - (E_{left} - E_0) \frac{x}{\lambda_N} \right] \\ &\quad + a E_0 \frac{u_d}{v_g} \left[ \left( \frac{x}{\lambda_N} \right)^2 - 1 \right], \end{aligned} \quad (64)$$

$$\begin{aligned} E(L-y) &= \frac{1}{2} \left[ E_{right} + E_0 + (E_0 - E_{right}) \frac{y}{\lambda_N} \right] \\ &\quad + a E_0 \frac{u_d}{v_g} \left[ 1 - \left( \frac{y}{\lambda_N} \right)^2 \right], \end{aligned} \quad (65)$$

$$\Delta E_{left} = E(x) - E_0 = \frac{4}{3} b \alpha \frac{u_d}{v_g} \left(1 + 2\alpha \frac{u_d}{v_g}\right) e^{-\frac{x}{\lambda}} E_0, \quad (66)$$

$$\Delta E_{right} = E(L-y) - E_0 = -\frac{4}{3} b \alpha \frac{u_d}{v_g} \left(1 + 2\alpha \frac{u_d}{v_g}\right) e^{-\frac{y}{\lambda}} E_0. \quad (67)$$

Here,  $a$  is set to be 0.24 and  $b$  is 0.16.  $c$  is 2.2. These models are compared with the hydrodynamic temperature profile with  $\lambda_N = 1000$  nm, as shown in Fig. 20. The particle propagation model predicts a quadratic function, depicting the temperature increase in the left boundary and the temperature decrease in the right

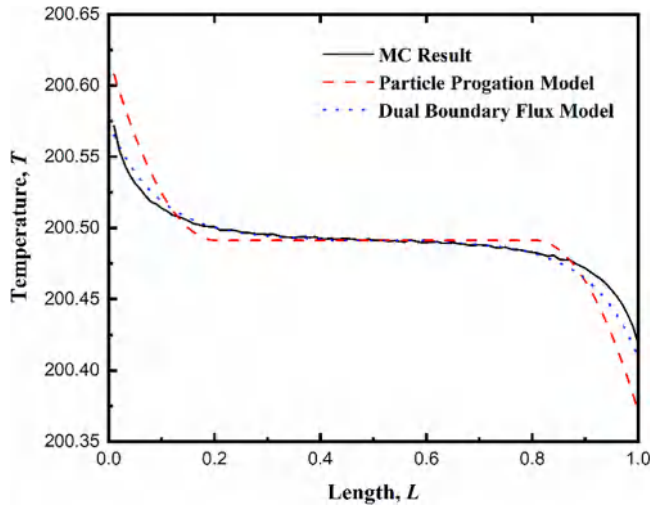


**FIG. 20.** Comparisons of the steady temperature distribution profiles in hydrodynamic heat conduction between the MC results and theoretical models.

boundary. However, the exponential function predicted by the dual boundary flux model seems to match the temperature profile better. These models describe the transition from non-collective distribution to collective distribution and the sources of thermal resistance.

#### D. Theoretical models for the interfacial temperature difference

Moreover, interfacial thermal resistance and its influences can also be understood by the dual boundary flux model. When the phonons meet the interface, some of them will be reflected while the others continue propagating forward, where the portion is determined by the interface roughness and material properties. The interface transmissivity  $t$  is defined to characterize the phonon proportion that can get through the interface. The transmissivity from the left side to the right side  $t_{12}$  and the one from the right side to the left side  $t_{21}$  can be different. If the materials at both sides of the interface are the same, the transmissivity at both sides is equal. The specular reflectivity  $s$  determines the ways that phonons are scattered at the interface. When specular reflectivity  $s = 1$ , the phonons meeting with the interface go back based on Fresnel's law. When  $s = 0$ , the phonons at the interface forget their previous state and are re-emitted with new information about the phonon branch, frequency, and wave vector. Similarly, the specular reflectivity of different interface sides might be different. Here, they are set to be equal,  $s_1 = s_2$ . When  $t = 1$  and  $s = 1$ , this model becomes the acoustic mismatch model. When  $t = 1$  and  $s = 0$ , the model reduces to the diffusive mismatch model.

The dual boundary flux can be adopted to establish the hydrodynamic interface model. The coarse interface means  $s = 0$ , and it emits the phonons as the diffusive heat flux. When the interface transmissivity is equal to 1, the phonon energy density that passes the interface can be written as the function of steady energy density  $E_0$ ,

$$q_{hydro} = q_{hydro| \cos \theta < 0} + (1 - s)q_{diff| \cos \theta > 0} \exp\left(-\frac{x}{\lambda}\right) + sq_{hydro| \cos \theta > 0} + (1 - s)q_{hydro| \cos \theta > 0} \left[1 - \exp\left(-\frac{x}{\lambda}\right)\right], \quad (68)$$

$$E_+(x) = \frac{E_0 - 2\alpha E_0 u_d / v_g}{2E_0} E_0 + \frac{E_0 + 2\alpha E_0 u_d / v_g}{2E_0} E_0 [(1 - s)(1 - e^{-x/\lambda}) + (1 - s)r_{E+} e^{-x/\lambda} + s]. \quad (69)$$

At that time, the steady energy density  $E_{01}$  in medium 1 is set to be equal to that in medium 2  $E_{02}$ . In the similar way, the phonon energy density at the left side of the interface is

$$E_-(x) = \frac{E_0 + 2\alpha E_0 u_d / v_g}{2E_0} E_0 + \frac{E_0 - 2\alpha E_0 u_d / v_g}{2E_0} E_0 [(1 - s)(1 - e^{-x/\lambda}) + (1 - s)r_{E-} e^{-x/\lambda} + s]. \quad (70)$$

The energy density difference between the left and right sides of the interface is

$$\Delta E = E_-(x) - E_+(x) = \frac{8}{3} \alpha \frac{v_d}{v_g} \left(1 + 2\alpha \frac{v_d}{v_g}\right) (1 - s) e^{-x/\lambda} E_0. \quad (71)$$

In the above model, the interface transmissivity is set to be 1. If not all the phonons can get through the interface and some go back to the previous medium, it leads to the difference between  $E_{01}$  and  $E_{02}$  in the two separate nanofilms,

$$\frac{E_{01}}{E_{02}} = \frac{2 - t}{t}. \quad (72)$$

Then, the energy difference at the interface is

$$\begin{aligned} \Delta E &= (E_{01} - \Delta E_1) - (E_{02} + \Delta E_2) \\ &= (2 - 2t)E_0 - \frac{4}{3} \alpha \frac{u_{d,1}}{v_g} \left(1 + 2\alpha \frac{u_{d,1}}{v_g}\right) (1 - s)E_1 \\ &\quad - \frac{4}{3} \alpha \frac{u_{d,2}}{v_g} \left(1 + 2\alpha \frac{u_{d,2}}{v_g}\right) (1 - s)E_2, \end{aligned} \quad (73)$$

where

$$E_{01} = (2 - t)E_0, \quad (74)$$

$$E_{02} = tE_0, \quad (75)$$

$$E_{01} u_{d,1} = E_{02} u_{d,2}. \quad (76)$$

When the phonon drift velocity is much smaller than the phonon group velocity, Eq. (73) can be simplified into

$$\Delta E = (2 - 2t)E_0 - \frac{8}{3}\alpha \frac{u_{d,1}}{v_g}(1 - s)(2 - t)E_0. \quad (77)$$

This equation gives a linear relation between the energy density difference and  $t$ ,  $s$ . When  $t = 1$  and  $s = 1$ , there is no difference. When  $s = 0$  and  $t = 0$ , the difference reaches maximum.

## V. CONCLUSIONS

Phonon hydrodynamic heat conduction, where the N process dominates, predicts many interesting physical phenomena, such as second sound and ultrahigh thermal conductivity. Two-dimensional materials have relatively larger hydrodynamic windows than bulk materials, where the N process plays an important role. As it is known, the N process causes no thermal resistance because it conserves the phonon momentum in heat transport. However, it can influence the thermal conductivity indirectly by the interactions with other mechanisms, such as the Umklapp scattering process and boundary scatterings. This article focuses on the boundary thermal behaviors and the interfacial thermal resistance in phonon hydrodynamic heat conduction. If the boundaries are thought to have ideal thermalized contacts, phonons propagating from one end to the other end will experience the transition from non-collective distribution to collective distribution, which results in thermal resistance. It is assumed that interfacial behaviors can be seen as the sum of the interactions in two separated nanofilms with the interface effects, which has been demonstrated to be reasonable via numerical simulations. The hydrodynamic interfacial thermal resistance is important in polycrystalline structures and material connections.

The thermal resistance in a finite length nanofilm is presented in two ways, namely, the hydrodynamic thermal resistance and the effective thermal resistance, since there is no temperature gradient in the middle part of the materials in steady hydrodynamic heat conduction. The normal scattering process leads to different heat conduction phenomena from ballistic heat transport. It is found that the heat flux decreases when the Knudsen number goes down. The boundary temperature step, denoting the temperature decline near the boundary, is demonstrated to have different behaviors under temperature boundary and heat flux boundary. Two theoretical models, i.e., the particle propagation model and the dual boundary flux model, are proposed to predict the heat flux reduction and temperature steps from different views. The particle propagation model considers the contribution of thermal energy distribution from the surroundings and derives a quadratic temperature profile. The dual boundary flux model divides the fluxes into hydrodynamic heat flux and diffusive heat flux and shows their different influences on heat conduction.

Due to the boundary temperature step, the interfacial thermal resistance can no longer be determined only from the temperature differences at the interface just as in diffusive heat conduction. Therefore, hydrodynamic interfacial thermal resistance is used to analyze the interface behaviors, which are characterized by the interface transmissivity  $t$  and the specular reflectivity  $s$ . Moreover, when the interface transmissivity  $t$  is large enough and specular reflectivity approaches 0, inverse temperature difference appears,

where it seems that the heat flux flows from low to high temperature. The dual boundary flux model is capable of predicting the temperature difference and the energy density difference at the interface.

When Umklapp scatterings become stronger, it gives important influences on the nanofilm thermal resistance and the whole heat transport process turns to the Ziman hydrodynamic regime. The coupled effects between the N and U processes can change the temperature profile and the boundary temperature step. It is widely applicable because pure Poiseuille hydrodynamic heat conduction is difficult to realize in common circumstances. The resistance scattering process always exists in nanoscale heat transport, such as ballistic-diffusive heat transport. Therefore, the investigations of the coupling effects of the N and U processes would benefit the heat conduction management in two-dimensional materials.

## ACKNOWLEDGMENTS

This work was financially supported by the National Natural Science Foundation of China (NNSFC) (Grant Nos. 51825601 and U20A20301).

## AUTHOR DECLARATIONS

### Conflict of Interest

The authors have no conflicts of interest to disclose.

## DATA AVAILABILITY

The data that support the findings of this study are available from the corresponding author upon reasonable request.

## REFERENCES

- <sup>1</sup>K. Khan, A. K. Tareen, M. Aslam, R. Wang, Y. Zhang, A. Mahmood, Z. Ouyang, H. Zhang, and Z. Guo, *J. Mater. Chem. C* **8**, 387 (2020).
- <sup>2</sup>N. Wang, M. K. Samani, H. Li, L. Dong, Z. Zhang, P. Su, S. Chen, J. Chen, S. Huang, G. Yuan, X. Xu, B. Li, K. Leifer, L. Ye, and J. Liu, *Small* **14**, 1801346 (2018).
- <sup>3</sup>U. Choudhry, S. Yue, and B. Liao, *Phys. Rev. B* **100**, 165401 (2019).
- <sup>4</sup>M. Xu, *Phys. Lett. A* **389**, 127076 (2021).
- <sup>5</sup>A. Alofi and G. P. Srivastava, *J. Appl. Phys.* **112**, 013517 (2012).
- <sup>6</sup>Y. Machida, N. Matsumoto, T. Isono, and K. Behnia, *Science* **367**, 309 (2020).
- <sup>7</sup>S. Lee, D. Broido, K. Esfarjani, and G. Chen, *Nat. Commun.* **6**, 6290 (2015).
- <sup>8</sup>A. Cepellotti, G. Fugallo, L. Paulatto, M. Lazzeri, F. Mauri, and N. Marzari, *Nat. Commun.* **6**, 6400 (2015).
- <sup>9</sup>B. N. Narozhny, I. V. Gornyi, M. Titov, M. Schütt, and A. D. Mirlin, *Phys. Rev. B* **91**, 035414 (2015).
- <sup>10</sup>C. Yu, Y. Ouyang, and J. Chen, *J. Appl. Phys.* **130**, 010902 (2021).
- <sup>11</sup>S. Lee and L. Lindsay, *Phys. Rev. B* **95**, 184304 (2017).
- <sup>12</sup>J. Callaway, *Phys. Rev.* **113**, 1046 (1959).
- <sup>13</sup>R. A. Guyer and J. A. Krumhansl, *Phys. Rev.* **148**, 766 (1966).
- <sup>14</sup>R. A. Guyer and J. A. Krumhansl, *Phys. Rev.* **148**, 778 (1966).
- <sup>15</sup>R. J. Hardy and D. L. Albers, *Phys. Rev. B* **10**, 3546 (1974).
- <sup>16</sup>A. K. Majee and Z. Aksamija, *Phys. Rev. B* **98**, 024303 (2018).
- <sup>17</sup>M. Markov, J. Sjakste, G. Barbarino, G. Fugallo, L. Paulatto, M. Lazzeri, F. Mauri, and N. Vast, *Phys. Rev. Lett.* **120**, 075901 (2018).
- <sup>18</sup>Z. Zhang, Y. Ouyang, Y. Guo, T. Nakayama, M. Nomura, S. Volz, and J. Chen, *Phys. Rev. B* **102**, 195302 (2020).
- <sup>19</sup>K. Ghosh, A. Kusiak, and J.-L. Battaglia, *Phys. Rev. B* **102**, 094311 (2020).

- <sup>20</sup>B. D. Nie and B. Y. Cao, *Nanoscale Microscale Thermophys. Eng.* **24**, 94 (2020).
- <sup>21</sup>A. Beardo, M. G. Hennessy, L. Sendra, J. Camacho, T. G. Myers, J. Bafaluy, and F. X. Alvarez, *Phys. Rev. B* **101**, 075303 (2020).
- <sup>22</sup>V. Martelli, J. L. Jimenez, M. Continentino, E. Baggio-Saitovitch, and K. Behnia, *Phys. Rev. Lett.* **120**, 125901 (2018).
- <sup>23</sup>M. Calvo-Schwarzwalder, M. G. Hennessy, P. Torres, T. G. Myers, and F. X. Alvarez, *Int. J. Heat Mass Transfer* **126**, 1120 (2018).
- <sup>24</sup>Y. Guo, Z. Zhang, M. Bescond, S. Xiong, M. Wang, M. Nomura, and S. Volz, *Phys. Rev. B* **104**, 075450 (2021).
- <sup>25</sup>M. Xu, *Proc. R. Soc. London, A* **477**, 20200913 (2021).
- <sup>26</sup>N. N. Zholonko, *Phys. Solid State* **48**, 1678 (2006).
- <sup>27</sup>Y. Machida, A. Subedi, K. Akiba, A. Miyake, M. Tokunaga, Y. Akahama, K. Izawa, and K. Behnia, *Sci. Adv.* **4**, eaat3374 (2018).
- <sup>28</sup>X. Li and S. Lee, *Phys. Rev. B* **97**, 094309 (2018).
- <sup>29</sup>S. Lee, X. Li, and R. Guo, *Nanoscale Microscale Thermophys. Eng.* **23**, 247 (2019).
- <sup>30</sup>C. C. Ackerman, B. Bertman, H. A. Fairbank, and R. A. Guyer, *Phys. Rev. Lett.* **16**, 789 (1966).
- <sup>31</sup>H. E. Jackson, C. T. Walker, and T. F. McNelly, *Phys. Rev. Lett.* **25**, 26 (1970).
- <sup>32</sup>V. Narayanamurti and R. Dynes, *Phys. Rev. Lett.* **28**, 1461 (1972).
- <sup>33</sup>D. W. Pohl and V. Irniger, *Phys. Rev. Lett.* **36**, 480 (1976).
- <sup>34</sup>R. Kovacs and P. Van, *Int. J. Heat Mass Transfer* **117**, 682 (2018).
- <sup>35</sup>X. P. Luo, Y. Y. Guo, M. R. Wang, and H. L. Yi, *Phys. Rev. B* **100**, 155401 (2019).
- <sup>36</sup>P. Scuracchio, K. H. Michel, and F. M. Peeters, *Phys. Rev. B* **99**, 144303 (2019).
- <sup>37</sup>S. Huberman, R. A. Duncan, K. Chen, B. Song, V. Chiloyan, Z. Ding, A. A. Maznev, G. Chen, and K. A. Nelson, *Science* **364**, 375 (2019).
- <sup>38</sup>J. Jeong, X. Li, S. Lee, L. Shi, and Y. Wang, *Phys. Rev. Lett.* **127**, 085901 (2021).
- <sup>39</sup>W.-J. Yao and B.-Y. Cao, *Chin. Sci. Bull.* **59**, 3495 (2014).
- <sup>40</sup>L. Lindsay, D. A. Broido, and N. Mingo, *Phys. Rev. B* **80**, 125407 (2009).
- <sup>41</sup>T. Feng, L. Lindsay, and X. Ruan, *Phys. Rev. B* **96**, 161201 (2017).
- <sup>42</sup>L. Lindsay, D. A. Broido, and N. Mingo, *Phys. Rev. B* **82**, 115427 (2010).
- <sup>43</sup>L. Shi, *Science* **364**, 332 (2019).
- <sup>44</sup>P. B. Allen, *Phys. Rev. B* **88**, 144302 (2013).
- <sup>45</sup>C. de Tomas, A. Cantarero, A. F. Lopeandia, and F. X. Alvarez, *J. Appl. Phys.* **115**, 164314 (2014).
- <sup>46</sup>R. Yang, S. Yue, and B. Liao, *Nanoscale Microscale Thermophys. Eng.* **23**, 25 (2018).
- <sup>47</sup>X. Li and S. Lee, *Phys. Rev. B* **99**, 085202 (2019).
- <sup>48</sup>Y. Dong, B. Y. Cao, and Z.-Y. Guo, *Physica E* **56**, 256 (2014).
- <sup>49</sup>E. T. Swartz and R. O. Pohl, *Rev. Mod. Phys.* **61**, 605 (1989).
- <sup>50</sup>W.-B. Lor and H. S. Chu, *Numer. Heat Transfer, Part A* **36**, 681 (1999).
- <sup>51</sup>B. D. Nie and B. Y. Cao, *Int. J. Heat Mass Transfer* **116**, 314 (2018).
- <sup>52</sup>E. S. Landry and A. J. H. McGaughey, *Phys. Rev. B* **80**, 165304 (2009).
- <sup>53</sup>K. Pietrak and T. S. Wisniewski, *J. Power Technol.* **94**, 270 (2014). <https://papers.itc.pw.edu.pl/index.php/JPT/article/view/462>
- <sup>54</sup>K. Ruan, X. Shi, Y. Guo, and J. Gu, *Compos. Commun.* **22**, 100518 (2020).
- <sup>55</sup>A. Giri and P. E. Hopkins, *Adv. Funct. Mater.* **30**, 1903857 (2019).
- <sup>56</sup>P. Zhang, P. Yuan, X. Jiang, S. Zhai, J. Zeng, Y. Xian, H. Qin, and D. Yang, *Small* **14**, 1702769 (2018).
- <sup>57</sup>Y. C. Hua and B. Y. Cao, *Nanoscale Microscale Thermophys. Eng.* **21**, 159 (2017).
- <sup>58</sup>P. L. Kapitza, *Phys. Rev.* **60**, 354 (1941).
- <sup>59</sup>I. M. Khalatnikov and I. N. Adamenko, *J. Exp. Theor. Phys.* **36**, 391 (1973).
- <sup>60</sup>M. Frank and D. Drikakis, *Microfluid Nanofluidics* **21**, 148 (2017).
- <sup>61</sup>M. Frank and D. Drikakis, *Entropy* **20**, 362 (2018).
- <sup>62</sup>M. Frank, M. Papanikolaou, D. Drikakis, and K. Salonitis, *J. Chem. Phys.* **151**, 134705 (2019).
- <sup>63</sup>C. Hua and A. J. Minnich, *J. Appl. Phys.* **117**, 175306 (2015).
- <sup>64</sup>Q. Hao, Y. Xiao, and Q. Chen, *Mater. Today Phys.* **10**, 100126 (2019).
- <sup>65</sup>W. B. Lor and H. S. Chu, *Int. J. Heat Mass Transfer* **43**, 653 (2000).
- <sup>66</sup>J. R. Ho, C. P. Kuo, and W.-S. Jiaung, *Int. J. Heat Mass Transfer* **46**, 55 (2003).
- <sup>67</sup>K. C. Liu, *Int. J. Heat Mass Transfer* **50**, 1397 (2007).
- <sup>68</sup>K. Ramadan and M. A. Al-Nimr, *Heat Transfer Eng.* **30**, 677 (2009).
- <sup>69</sup>K. Ramadan and M. A. Al-Nimr, *J. Heat Transfer* **130**, 074501 (2008).
- <sup>70</sup>K. Ramadan and M. A. Al-Nimr, *Int. J. Therm. Sci.* **48**, 1718 (2009).
- <sup>71</sup>A. Alofi and G. P. Srivastava, *Phys. Rev. B* **87**, 115421 (2013).
- <sup>72</sup>J.-P. M. Peraud, C. D. Landon, and N. G. Hadjiconstantinou, *Annu. Rev. Heat Transfer* **17**, 205 (2014).
- <sup>73</sup>Y. C. Hua and B. Y. Cao, *Int. J. Heat Mass Transfer* **78**, 755 (2014).
- <sup>74</sup>Y. C. Hua and B. Y. Cao, *Nanoscale Microsc. Therm.* **21**, 159 (2017).
- <sup>75</sup>S. Mei, L. N. Maurer, Z. Aksamija, and I. Knezevic, *J. Appl. Phys.* **116**, 164307 (2014).
- <sup>76</sup>J. Sussmann and A. Thellung, *Proc. Phys. Soc.* **81**, 1122 (1963).